Cell Reports

Article

Energy Scarcity Promotes a Brain-wide Sleep State Modulated by Insulin Signaling in *C. elegans*

Graphical Abstract

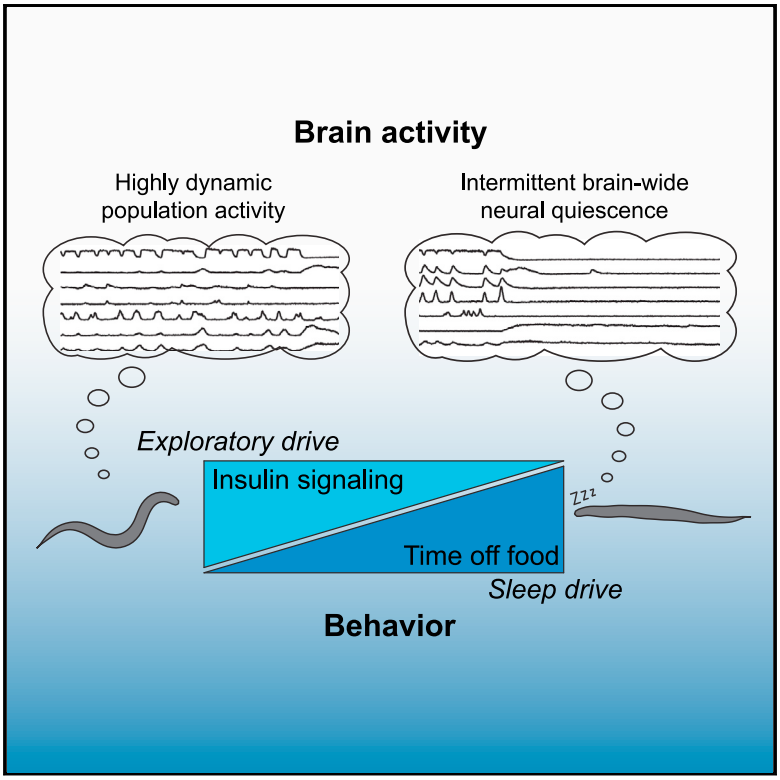

Authors

Susanne Skora, Fanny Mende, Manuel Zimmer

Correspondence

manuel.zimmer@imp.ac.at

In Brief

Skora et al. show in *C. elegans* that upon acute food deprivation, insulin signaling contributes to transient arousal, which declines with long-term starvation, hence permitting episodic sleep. During the remaining episodes of wakefulness, the brain maintains dynamic network activities. Sleep thus potentially serves an adaptive function in response to energy scarcity.

Highlights

- Starvation shifts the behavioral strategy from exploration to intermittent sleep
- Brain-wide neuronal population dynamics are robust to starvation
- Neuromodulation via insulin signaling maintains wakefulness during short fasting
- The insulin receptor DAF-2 acts in a network of sensory neurons and interneurons

Skora et al., 2018, Cell Reports *22*, 953–966
January 23, 2018
https://doi.org/10.1016/j.celrep.2017.12.091

CellPress

Cell Reports
Article

Energy Scarcity Promotes a Brain-wide Sleep State Modulated by Insulin Signaling in *C. elegans*

Susanne Skora,[1] Fanny Mende,[1,2] and Manuel Zimmer[1,3,*]
[1]Research Institute of Molecular Pathology (IMP), Vienna Biocenter (VBC), Campus-Vienna-Biocenter 1, 1030 Vienna, Austria
[2]Present address: Roche Pharmaceutical Research and Early Development, Roche Innovation Center Zurich, Roche Glycart AG, Wagistrasse 10, 8952 Schlieren, Switzerland
[3]Lead Contact
*Correspondence: manuel.zimmer@imp.ac.at
https://doi.org/10.1016/j.celrep.2017.12.091

SUMMARY

Neural information processing entails a high energetic cost, but its maintenance is crucial for animal survival. However, the brain's energy conservation strategies are incompletely understood. Employing functional brain-wide imaging and quantitative behavioral assays, we describe a neuronal strategy in *Caenorhabditis elegans* that balances energy availability and expenditure. Upon acute food deprivation, animals exhibit a transiently elevated state of arousal, indicated by foraging behaviors and increased responsiveness to food-related cues. In contrast, long-term starvation suppresses these behaviors and biases animals to intermittent sleep episodes. Brain-wide neuronal population dynamics, which are likely energetically costly but important for behavior, are robust to starvation while animals are awake. However, during starvation-induced sleep, brain dynamics are systemically downregulated. Neuromodulation via insulin-like signaling is required to transiently maintain the animals' arousal state upon acute food deprivation. Our data suggest that the regulation of sleep and wakefulness supports optimal energy allocation.

INTRODUCTION

The evolution of brains is constrained by the need for energy efficiency (Laughlin, 2001), yet brains remain among the most energy-consuming organs (Mink et al., 1981). This peculiarity of nervous systems might originate from a fundamental physical principle (Landauer's principle) that assigns a lower bound of energy consumption to computations (Landauer, 1961), rendering information-processing systems, such as brains, energetically costly. Therefore, brain operations must be contingent upon a tight balance between energy expenditure and conservation. Although there is an increasing body of knowledge delineating the brain circuitries that regulate appetite, food intake, and metabolism (Waterson and Horvath, 2015), much less is known about adaptive neuronal mechanisms that govern energy efficiency of neuronal processing.

Previous studies in insects suggest that neuronal processing is compromised when energy supply is scarce (Longden et al., 2014; Plaçais and Preat, 2013). Acute food deprivation in flies enhances arousal (Keene et al., 2010), but resistance to chronic starvation is associated with increased sleep (Slocumb et al., 2015). A similar yet less well-defined transition from initial arousal to elevated sleep levels is reported for rodents (Alvarenga et al., 2005), suggesting common adaptive mechanisms across animal phyla. However, the underlying systemic changes in neuronal activity patterns, and the neuromodulatory pathways that could regulate such neuronal adaptations are largely unknown. We propose here that studying behavior and brain activity under a strict regime of energy deprivation should directly reveal such adaptive mechanisms.

The nematode *C. elegans* is ideally suited for such studies. An array of behavioral paradigms has been established to measure behavioral adaptations to food deprivation; among these are chemotactic responses to ambient oxygen (O_2) levels (Zimmer et al., 2009). *C. elegans* inhabits rotten material in soil (Frézal and Félix, 2015), an environment where local fluctuations in O_2 potentially indicate the presence of bacterial food (Gray et al., 2004; Hums et al., 2016; Sexstone et al., 1985). Action commands are encoded in the worm brain by coordinated neuronal network dynamics, involving approximately 40% of all head neurons (Kato et al., 2015; Schrödel et al., 2013). These dynamics are systemically downregulated during developmentally timed sleep (termed lethargus) (Nichols et al., 2017). Taken together, these studies suggest that arousal and sleep in worms largely differ in their energy demands.

Here, we show that progressive energy deprivation of *C. elegans* is associated with an initial state of arousal followed by increasing pressure to enter reversible episodes of sleep. Unexpectedly, brain-wide network dynamics are robust to energy scarcity following starvation but become interspersed with short episodes of sleep. These data suggest that network dynamics are critical for neuronal function and that short bouts of sleep contribute to energy conservation, by reducing both brain and muscle activity. Starvation-induced sleep requires the FOXO transcription factor DAF-16. Its inhibition via the conserved insulin/IGF-1 pathway in a sensory neuron-interneuron network suppresses sleep during the initial arousal phase. We propose that neuromodulatory control of sleep and arousal via insulin signaling serves as an adaptive strategy to cope with energy deficits.

RESULTS

Arousal State Changes over the Time Course of Food Deprivation

We employed a previously reported population assay in which worms crawling freely on agarose perceive rapid temporal shifts in O_2 concentration from atmospheric 21% to intermediate 10% O_2 (henceforth "O_2 downshift") (Zimmer et al., 2009). Using this paradigm, we previously reported that 1-hr food-deprived worms (henceforth "fasted") elicit a sustained switch in behavioral strategy from long-distance travel (LDT) prevalent at 21% O_2 to sustained area-restricted search (ARS)-like behavior at 10% O_2 (Hums et al., 2016). A food deprivation time course that extends from 15 min off food ("well-fed") to severe starvation (16 hr off food, "starved") revealed a gradual change in behavioral strategy (Figures 1A–1D and S1A): whereas well-fed animals only briefly reduced locomotion speed in response to O_2 downshift (Figures 1A and 1B), fasted animals exhibited the prolonged slowing and backward-crawling (reversal) response previously extensively characterized as ARS behavior (Figures 1A and 1B) (Hums et al., 2016). This difference in fasted versus well-fed behavior demonstrates an enhanced behavioral responsiveness of fasted animals toward intermediate O_2 concentrations. As a condition of severe starvation, we chose 16 hr off food. At this point, animals have already largely reduced their fat resources (Witham et al., 2016) and retained eggs. However, larvae did not yet hatch internally, which could impact the mother animals. Upon starvation, the O_2 downshift-evoked reversal response was attenuated and slowing was sustained, i.e., no speed recovery was observed throughout the 6-min period at low O_2 (Figures 1A and 1B). In addition, starved animals responded to O_2 downshift with transient episodes of motor inactivity that either affected the whole body (henceforth "quiescence") (Figure 1C), or were characterized by retained movement of the head-neck region (henceforth "head-waving") (Figures 1D and S1B; Movie S1). While quiescence was defined as a discrete behavioral state by the absence of any motion above the detection threshold of our method, we observed a smooth change in movement parameters from active forward crawling to head-waving (Figure S1C). Such a gradual adjustment of movement parameters was described previously (Gallagher et al., 2013; Hums et al., 2016). However, in order to quantify in parallel all observed behavioral features, in the present study we simplify and treat head-waving as a discrete category. Here, head-waving is defined by the absence of detectable crawling while movement remains apparent in anterior body parts (Figure S1B; Movie S1; see also Experimental Procedures). Quiescence and head-waving were immediately and completely suppressed by a subsequent O_2 upshift to 21%. Well-fed and fasted animals lacked quiescence and head-waving (Figures 1C and 1D).

In summary, during a food deprivation time course animals initially increased arousal levels, evidenced by elevated behavioral responsiveness, which was followed by a progressive propensity to enter reversible episodes of quiescence.

A Sensory Circuit Involved in O_2 Modulation of Starvation Quiescence

We next used genetic cell ablation strains to probe the neural requirements for quiescence and head-waving behavior in response to O_2 shifts. O_2 downshift activates O_2-sensory neurons of the BAG class (Zimmer et al., 2009), whereas O_2 upshift activates sensory neurons of the URX, AQR, and PQR classes (Persson et al., 2009; Zimmer et al., 2009). Surprisingly, quiescence was independent of BAG neurons but depended strongly on URX, AQR, and PQR neurons. Ablating all of these classes of O_2-sensing neurons did not suppress quiescence further (Figure S1D). RMG interneurons are central to a gap junction circuit of nociceptive, pheromone, and URX O_2 sensory neurons (Macosko et al., 2009) (Figure S1F). This circuit was shown to relay arousal signals from nociceptive (Choi et al., 2015) and O_2-sensory neurons (Nichols et al., 2017). Animals lacking RMG neurons showed reduced quiescence (Figure S1D) and head-waving (Figure S1E). Notably, the RMG cell ablation was the only one that affected O_2 downshift modulation of head-waving behavior (Figure S1E). Almost complete suppression of both quiescence and head-waving could be achieved by broadly disrupting sensory neuron-dependent signaling using animals mutant in the transient receptor potential channel V (TRPV) OSM-9 (Colbert et al., 1997) (Figures S1D and S1E). This indicates that sensory signals, likely from several neurons, are necessary for quiescence and head-waving episodes. The effect of RMG ablation on head-waving might thus be explained by either its role as a hub neuron downstream of several *osm-9*-expressing sensory neurons (Figure S1F) or via its potential role as motor neuron innervating muscles in the head (White et al., 1986). Surprisingly, none of the known O_2 upshift-sensing neurons and molecular O_2 upshift sensors was required for the acute arousal response upon O_2 upshift (Figure S1G).

In summary, starvation quiescence is under control of a sensory neuron-interneuron network including the hub interneuron RMG.

Acute Changes in Ambient O_2 Levels Transiently Modulate Behavioral State Transitions

In accordance with previous studies (Ghosh and Emmons, 2008; McCloskey et al., 2017), we found that starvation-induced quiescence also occurred independent of acute O_2 switches when animals were left unperturbed in the absence of food for at least 10 hr at constant 21% O_2 (Figure S2A). Furthermore, in longer-term (130-min) experiments on prior starved animals, quiescence was initially suppressed but reached steady-state levels after ~30 min (Figures 1E and 1F). This indicated that intermediate O_2 concentrations as used in our initial experiments (Figures 1A–1D) were likely to serve a modulatory function for a default starvation-dependent behavior rather than being permissive. It furthermore suggested that the handling prior to experiment start (i.e., moving of assay plates and initiation of O_2 flow) caused transient arousal of the worms. Once steady-state levels of quiescence had been established, acute O_2 downshifts or upshifts transiently modulated quiescence and head-waving behavior (Figures 1E and 1F).

We next used the identification of active, quiescent, and head-waving episodes to investigate the sequences of behavioral transitions and their modulation by O_2 shifts. Using the experiments shown in Figures 1E and 1F, we calculated state transition rates during steady-state periods at both 21% and 10% O_2, and upon O_2 shifts. The only significant difference between steady states

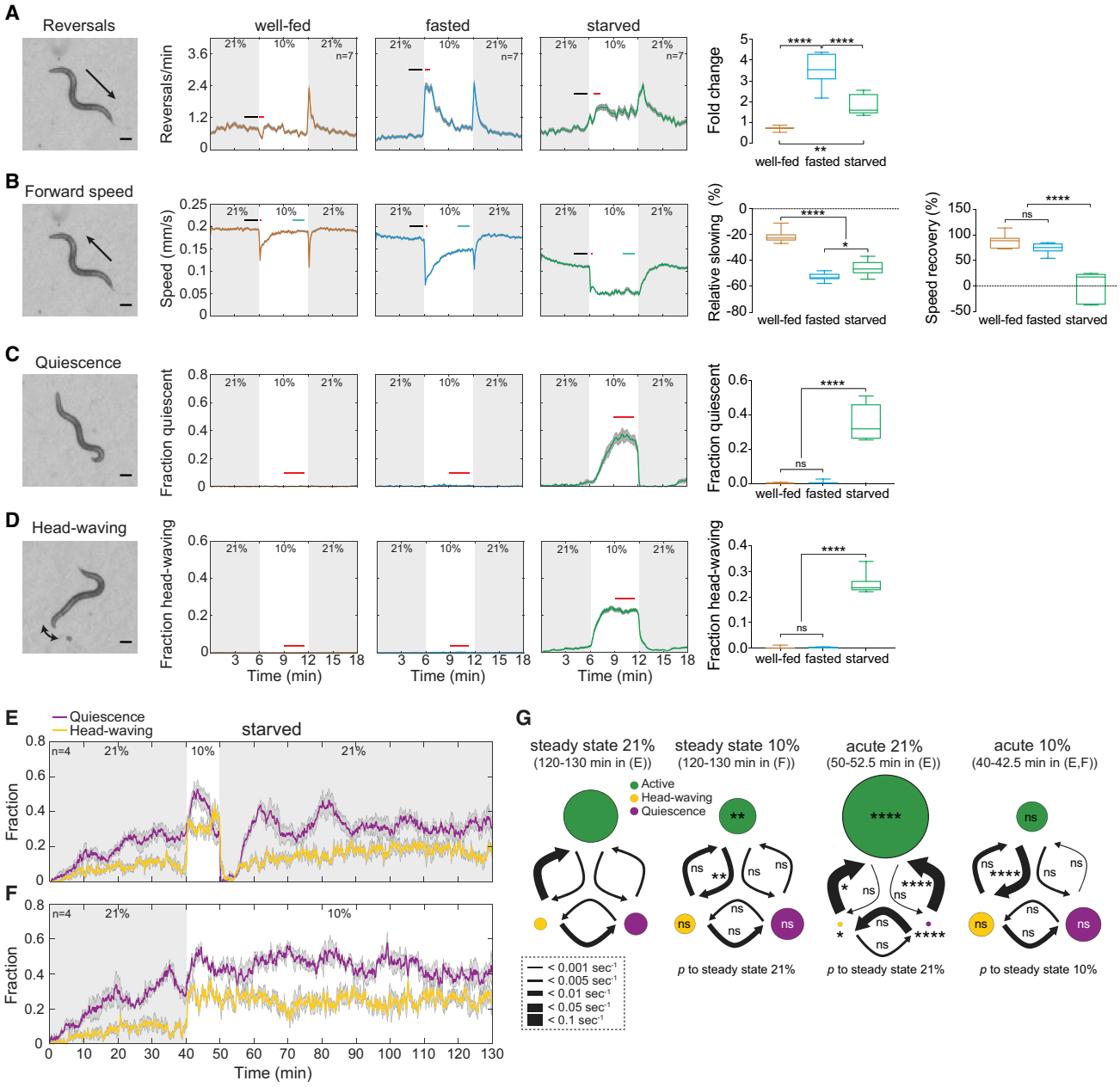

Figure 1. Change in Arousal State over the Time Course of Food Deprivation

(A–D) Pictures on the left show single video frames of WT worms during indicated behavior. Scale bars: 100 μm. Traces show population means (±SEM) across experiments under indicated feeding states for reversals (A), forward speed (B), quiescence (C), and head-waving behaviors (D). Animals were stimulated with changing O_2 concentrations as shown. n indicates number of experiments (~100 animals each). Bars denote time intervals used for quantifications on the right. Boxplots (median, interquartile range, and min to max whiskers) on the right show quantifications of fold- or %-change (red- versus black-labeled intervals) in reversal frequency and speed. Speed recovery is the %-change during cyan- versus red-labeled intervals relative to basal levels (black bar). Mean fraction quiescent or head-waving during red-labeled intervals. One-way ANOVA with Tukey's correction was used to compare all conditions against each other (****$p < 0.0001$, ***$p = 0.0009$, **$p = 0.0019$; ns, $p > 0.05$).

(E and F) Population means (±SEM) of fraction starved WT worms in quiescent (purple) or head-waving (yellow) state during longer recordings. O_2 concentration as indicated. n indicates number of experiments (~50 animals each). (F) Same as (E) but using different O_2 stimulation, as indicated.

(G) State transition rates calculated from (E) and (F). Arrow thickness show mean outbound transition rates according to legend in dashed box. Diameter of circles: mean state probability. Conditions were compared as indicated below panels using multiple t tests with Holm-Sidak correction (****$p < 0.0001$, **$p \leq 0.01$, *$p \leq 0.05$; ns, $p > 0.05$).

See also Figures S1 and S2 and Movie S1.

at chronic 10% versus 21% O_2 was an increase in the transition rate from active locomotion to head-waving (Figure 1G). Acute O_2 downshift further increased the transition rate from activity to head-waving while leaving other state transition rates unchanged. Thus, O_2 downshift promoted quiescence solely by elevating the prevalence of the head-waving state, which could thus be interpreted as a permissive prior state for quiescence (Figure 1G) that leads to a typical behavioral sequence of active → head-waving → quiescence. O_2 upshift affected all measured transitions, causing active locomotion to transiently prevail (Figure 1G). In conclusion, acute changes in ambient O_2 levels transiently modulated the extent of quiescence with respect to pre-stimulus levels, but none of the concentration ranges tested in this study was either strictly permissive or prohibitive for quiescence.

Starvation Quiescence Is a Behavioral Sleep State

Previously reported quiescent states in *C. elegans* fulfil criteria for sleep: reversibility, locomotion and feeding quiescence, specific posture, increased arousal thresholds, and homeostasis (Hill et al., 2014; Iwanir et al., 2013; Raizen et al., 2008). An assessment of whether starvation quiescence qualifies as sleep state, however, has been lacking. Reversibility occurred either via spontaneous switching (Figure 1G) or following O_2 upshift (Figure 1C). We next inspected feeding, i.e., pharyngeal pumping activity, in individual starved animals under a stereomicroscope and observed that, unlike during active or head-waving episodes, quiescence was devoid of feeding (Figure S2B).

We measured body postures via a shape factor (eccentricity) and found that quiescent worms were more straightened than worms during forward movement (Figure S2C).

Upon O_2 upshift, active worms responded with a strong acute reversal response whereas quiescent worms solely resumed to baseline reversal rates (Figure S2D), indicating reduced sensory responsiveness.

We found a small but highly significant correlation between the lengths of quiescence bouts and preceding active bouts (Figure S2E), indicating a minor homeostatic component to the quiescence drive. Notably, no significant correlation was found between other combinations of successive behavioral states (Figures S2F–S2H).

In conclusion, starvation quiescence fulfils the behavioral criteria to classify as sleep.

The Insulin Receptor DAF-2 Acts in a Sensory Neuron-Interneuron Network to Maintain an Arousal State upon Fasting

We conducted a candidate genetic screen in fasted animals and identified mutant strains showing quiescence prematurely upon fasting (Table S1). The most intriguing gene was *daf-2*, which encodes for the sole *C. elegans* homolog of the insulin/IGF-1 receptor (Kimura et al., 1997). Insulin signaling is known to affect quiescent states in both developing and adult animals (Gems et al., 1998) and has recently been suggested to modulate quiescence behavior in starved animals (McCloskey et al., 2017). Under our conditions, the *daf-2* mutation specifically affected the timescale of behavioral adaptation to food deprivation: *daf-2* fasted animals behaved like wild-type (WT) starved animals (Figures 2A and S3A). *Daf-2* animals have been reported to have reduced food ingestion rates (e.g., Dillon et al., 2016; Dwyer and Aamodt, 2013; McCloskey et al., 2017), a defect that could result in a chronic starvation state and lead to the display of a starved behavioral phenotype. However, quiescence of *daf-2* animals required the 1-hr off-food fasting period as it was not observed when well-fed (Figure 2A). Furthermore, our candidate genetic screen included animals with severe reductions in food intake (*eat-2* [Raizen et al., 1995], *tph-1* [Sze et al., 2000]), which did not display quiescence (Table S1). Nevertheless, we assayed feeding rates in *daf-2* animals under our cultivation conditions and found that *daf-2* mutants displayed only a mild reduction in pharyngeal pumping frequency (Figure S3B). These findings suggest that reduced food ingestion is insufficient to cause the phenotype observed in *daf-2* fasted animals and that *daf-2* plays rather a direct role in the regulation of quiescence behavior. One major output of the *daf-2* signaling pathway is the FOXO transcription factor *daf-16*. Consistent with DAF-2 signaling inhibiting FOXO (Kimura et al., 1997), quiescence levels in fasted *daf-16; daf-2* double mutants corresponded to *daf-16* levels (Figures 2B and S3C). Moreover, both *daf-16* single and *daf-16;daf-2* double mutants exhibited low levels of quiescence upon starvation (Figure 2B), indicating that high *daf-16* signaling, i.e., low levels of *daf-2* signaling, are required for elevated sleep upon starvation. This genetic evidence strongly supports our interpretation that insulin signaling maintains a transient aroused state upon fasting and that a progressive decline in insulin signaling leads to elevated sleep levels upon starvation.

Daf-2 is widely expressed across tissues (Cao et al., 2017); however, as assessed by transgenic rescue experiments using tissue-specific promoter fragments, maintenance of ARS behavior, indicated by sustained reversal and slowing responses, as well as arousal upon fasting could be restored by *daf-2* expression solely in the nervous system (using *Prab-3*) (Figures 2C and S3D). More specifically, arousal upon fasting could be partially restored by expressing *daf-2* either broadly in interneurons and motor neurons (using *Pglr-4*) or broadly in sensory neurons (using *Posm-9*, Figure 2C). The expression patterns of the *Pglr-4* and *Posm-9* promoters were assessed by confocal microscopy, yielding no overlap, and thus indicating that *daf-2* acts in a network that involves both sensory and interneurons. The top candidate neuron expressed under *Pglr-4* is the hub interneuron RMG. Expressing *daf-2* in RMG and a few other cells (using *Pflp-21*) restored quiescence levels similarly to *Pglr-4*. Expressing *daf-2* under both *Pflp-21* and *Posm-9* restored quiescence to levels comparable to WT (Figure 2C). Since *Pflp-21* and *Posm-9* overlapped in their expression in ASJ, ASJ is likely not critical for the observed additive effect. Exclusive expression of *daf-2* in URX, AQR, PQR, and ASI failed to affect quiescence (Figure S3E). We were unable to exclude significance of expression in URA or FLP, the only neurons besides RMG that were expressed under both *Pflp-21* and *Pglr-4*; however, the requirement of RMG for starvation-induced quiescence behavior (Figure S1D) and in the mediation of other arousal signals (Choi et al., 2015; Nichols et al., 2017) makes it a more likely candidate as a major site of *daf-2* action.

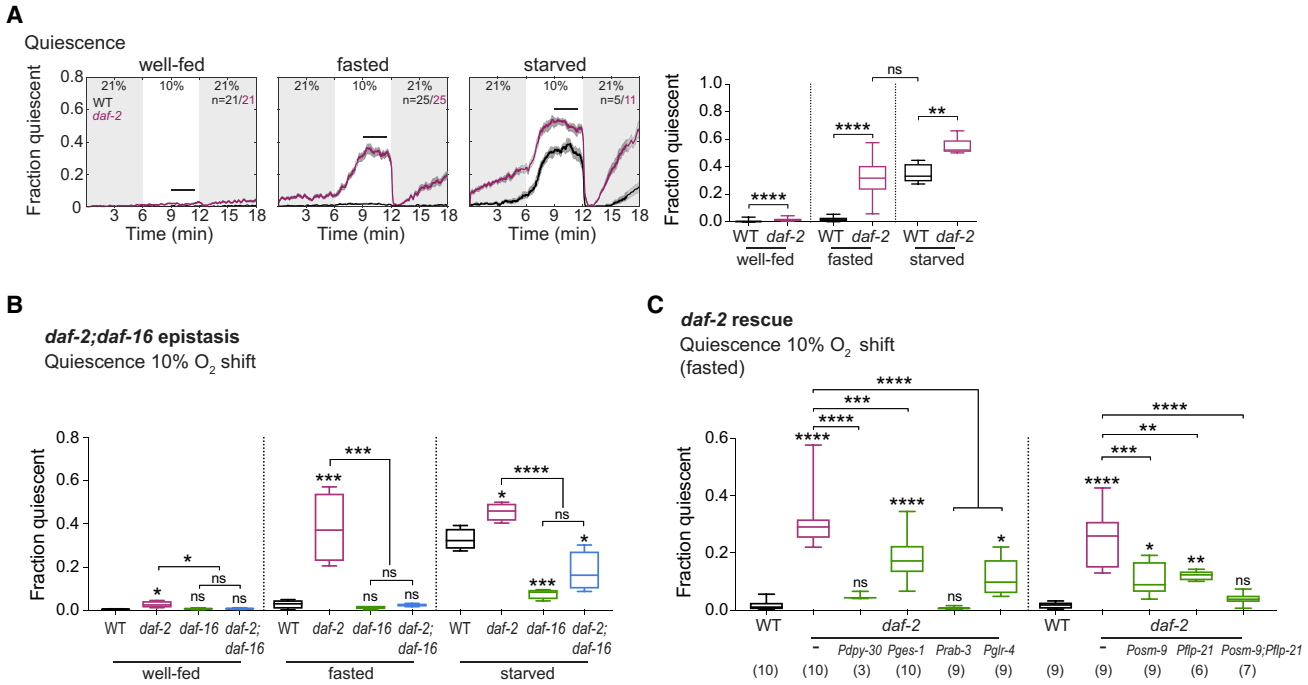

Figure 2. The Insulin Receptor DAF-2 Acts in a Sensory Neuron-Interneuron Network to Maintain Arousal upon Fasting

(A) Left: population means (±SEM) of quiescence behavior with O_2 stimulation under indicated feeding states. n indicates number of experiments (40–120 animals each). Right: quantifications using Mann-Whitney test (well-fed) or unpaired t test (others) (****$p < 0.0001$, **$p = 0.0018$; ns, $p = 0.7314$). n-numbers as indicated on the left, except *daf-2* starved, where only experiments performed in parallel to WT were used for quantification (i.e., n = 5).

(B) Quantification of *daf-2;daf-16* epistasis experiment for O_2 downshift-dependent quiescence under indicated feeding states, using one-way ANOVA with Tukey's correction (****$p < 0.0001$, ***$p < 0.001$, *$p \leq 0.05$; ns, $p > 0.05$). Significance against WT indicated above each boxplot. Additional comparisons as shown. Quantification interval as in Figure 2A. Number of experiments (n) = 4 each.

(C) Quantification of tissue- and cell-specific *daf-2* rescue experiments. *Pdpy-30*, ubiquitous; *Pges-1*, intestine; *Prab-3*, pan-neuronal; *Pglr-4*, interneurons and motor neurons; *Posm-9*, sensory neurons; *Pflp-21*, RMG, FLP, ASJ, M2, URA, URX, and ASI. Significance against WT indicated above each boxplot. Additional comparisons as shown. One-way ANOVA with Sidak's correction ****$p < 0.0001$, ***$p \leq 0.001$, **$p \leq 0.01$, *$p \leq 0.05$; ns, $p > 0.05$. Number of experiments (~40 animals each) below each boxplot.

WT and *daf-2* in (B) and (C) (left side) were controls performed in parallel but are subsets of the data in (A). WT and *daf-2* in (C) (right side) constitute a separate dataset. Boxplots show median, interquartile range, and min to max whiskers. See also Figure S3 and Table S1.

In summary, we identified the requirement for insulin signaling in both sensory neurons and interneurons in maintaining transient arousal upon fasting.

Starvation Promotes Periods of Global Neural Inactivity

We next sought to characterize the changes in brain activity that underlie the longer-timescale changes in behavior mediated by feeding state. We used a recently developed approach for brain-wide single-cell-resolution real-time Ca^{2+} imaging (Kato et al., 2015; Schrödel et al., 2013). Animals were immobilized in a microfluidic device allowing for high-resolution fluorescence microscopy and precise control of the gaseous environment (Zimmer et al., 2009). We previously reported that the brain activity of well-fed WT worms is dominated by global neuronal population dynamics, which arise from the coordinated activity involving a large fraction of all interneurons and motor neurons in the brain. Our previous work showed that these dynamics coordinate the generation of motor commands independent of movement, e.g., while animals are immobilized on the microscope stage (Kato et al., 2015). Here, we focused our efforts on the fasted and starved time points in order to characterize the changes in brain activity that underlie the frequent alternations between sleep and wakefulness. The imaging experiments employed the same protocol as used for behavioral experiments to switch between 21% and 10% O_2. We observed that starved, as opposed to fasted, worms frequently displayed periods of widespread downregulation of neuronal activity (Figures 3A–3C, S4A, and S4B). We used the brain state classifier validated during our previous work on lethargus sleep to quantify the occurrence of the episodes of neuronal downregulation: simultaneous inactivity of the AVA interneurons and the VB, SMD, and RIV motor neurons is a sufficient indicator of brain state episodes devoid of motor commands (Nichols et al., 2017). Applying this classifier to multiple recordings revealed that starvation was associated with an increased frequency of reversible quiescent brain state episodes (Figure 3D). While our imaging experiments recapitulated the frequent occurrence of quiescence upon starvation, we were unable to observe additional modulation by O_2 stimuli (compare Figures 3D and 3E). Similarly, we found that the O_2 stimulus did not elicit additional reversal commands (Figure S5). This is in contrast to our previous studies in well-fed animals, where we observed efficient stimulus-evoked motor

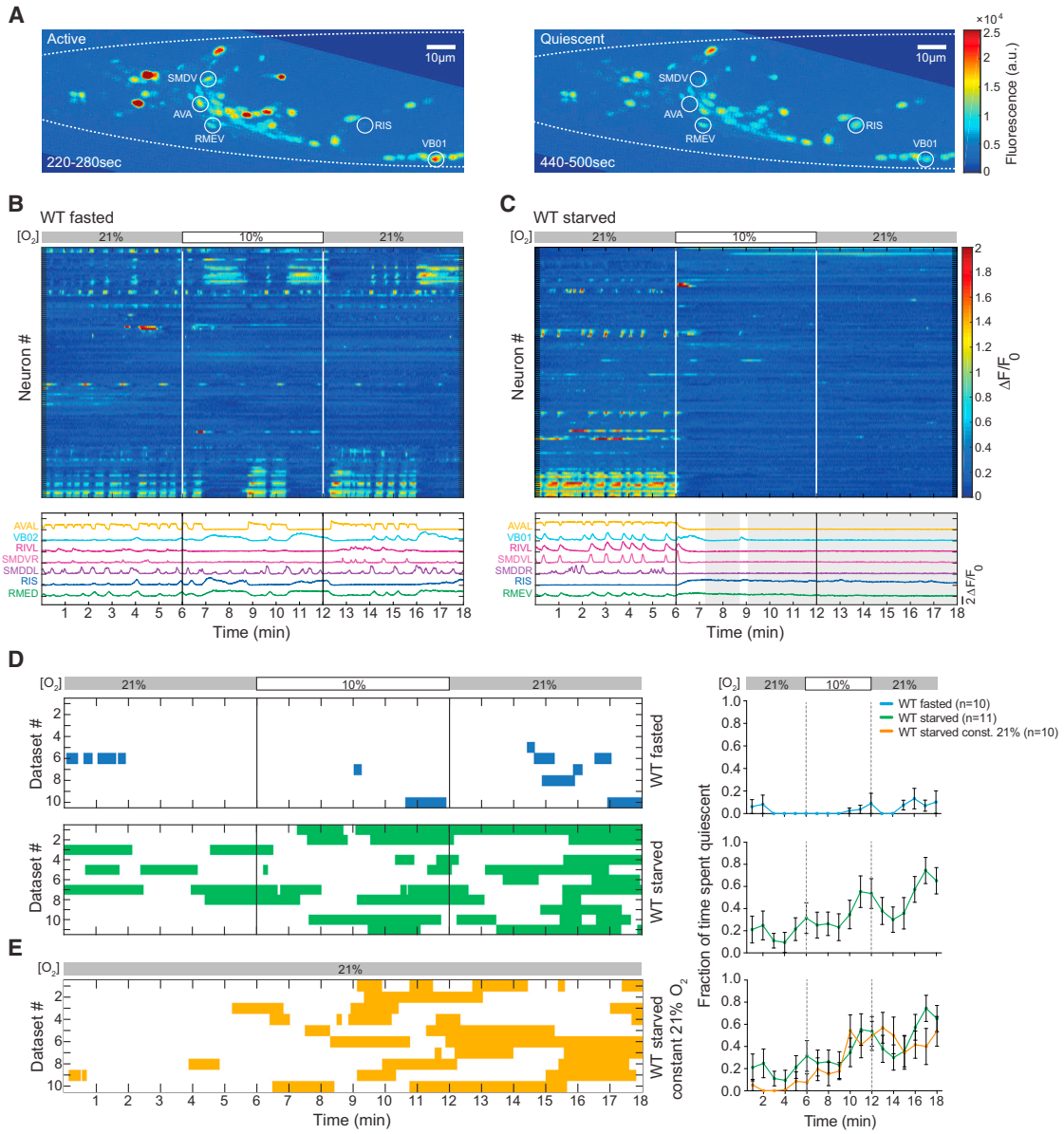

Figure 3. Starvation Promotes Episodes of Global Neural Inactivity

(A) Maximum intensity projections across the indicated time periods of the brain-wide imaging recording shown in (C). Selected neuronal classes are labeled.

(B and C) Heat plots of representative brain-wide imaging recordings for WT fasted (B) and WT starved (C) worms. O_2 stimulation as indicated. Rows are NLS-GCaMP5K fluorescence time series ($\Delta F/F_0$) of segmented head neurons, sorted by correlations. Example traces are shown below: reversal interneuron AVA, forward motor neurons VB02 or VB01, turning head motor neurons RIV, SMDV, and SMDD, and GABAergic neurons RIS and RMED/V. Grey shadings indicate quiescence periods.

(D and E) Left: brain state ethograms showing quiescence episodes of worms in brain-wide imaging recordings with O_2 stimulation as indicated. One row corresponds to one recording, each a different animal. Right: traces show mean (±SEM) fraction of time spent quiescent in 1-min bins, across all corresponding datasets shown on the left. n indicates number of recordings. (E) Same as (D) but at constant 21% O_2. Green traces in (D) and (E) on the right are the same data.

See Figures S4 and S5.

commands (Kato et al., 2015; Nichols et al., 2017). It is possible that fasted and starved worms are more affected by the confinement conditions in the device, leading to inefficient sensory-motor processing. Quiescence levels observed under these imaging conditions, however, followed a time course observed under basal freely behaving conditions (compare Figures 3D and 3E to first 20 min in Figures 1E and 1F). Therefore, our imaging results are most informative in the context of basal starvation quiescence but less so for O_2 modulation of quiescence behavior.

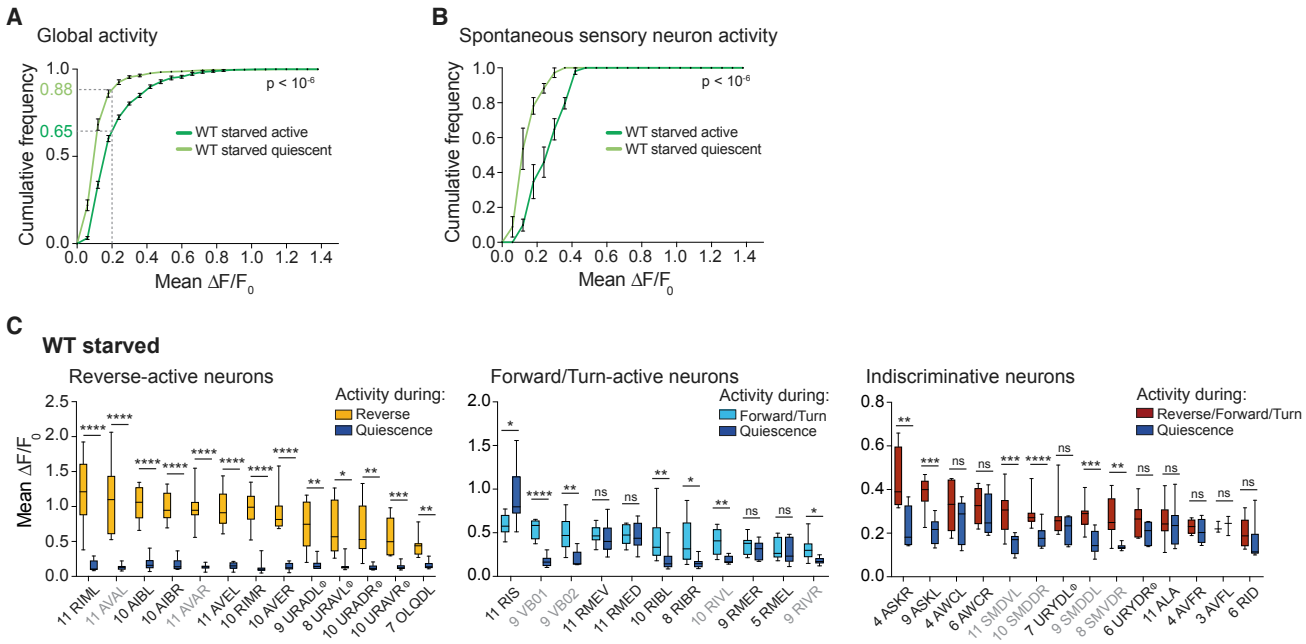

Figure 4. Sleep upon Starvation Recapitulates a Global Sleep Brain State

(A) Mean (±SEM) cumulative fractional distributions of mean $\Delta F/F_0$ values across all neurons (excluding O_2-responsive neurons) during active or quiescent episodes, in WT starved animals. Dashed gray lines denote a cutoff, below which neurons were usually found inactive. Number of recordings (n) = 6.

(B) Mean (±SEM) cumulative fractional distributions of mean $\Delta F/F_0$ values across spontaneously active sensory neurons during active or quiescent episodes. Number of recordings (n) = 6. The p values in (A) and (B) indicate the probability of obtaining an equal or higher difference between the distributions after random shuffling of quiescence episodes; see Experimental Procedures.

(C) Mean $\Delta F/F_0$ values of identified neurons during each neuron's principal active brain state (reverse, forward/turn, or active irrespective of motor state) and the quiescent brain state. Boxplots show median, interquartile range, and min to max whiskers. Labels indicate putative neuron IDs. Ambiguous IDs are labeled with Φ (see Experimental Procedures for alternatives). Number of data points for each neuron (n) indicated. Grayed neuronal classes were used for classification of quiescent brain states. Paired t tests (****$p < 0.0001$, ***$p \leq 0.001$, **$p \leq 0.01$, *$p \leq 0.05$; ns, $p > 0.05$).

See also Figure S6.

Starvation Quiescence Features a Global Sleep Brain State

We continued to investigate the quiescent brain state in depth, to compare it to the recently described sleep brain state during lethargus. As a global measure of neuronal activity changes from active to quiescent brain episodes, we compared the cumulative distributions of mean $\Delta F/F_0$ values for all neurons, except O_2-responsive neurons, in WT starved worms. This analysis quantitatively confirmed our initial observation (see Figures 3A–3C and S4B) that quiescence resulted in a downregulation of neuronal activity on a global scale (Figure 4A). Specifically, during active brain states, around ~35% of neurons were engaged in neuronal activity while this number was decreased to ~10% during quiescence. This downregulation thus affected approximately three-quarters of all typically active neurons. Since neuronal population dynamics in *C. elegans* encode motor commands, the suppression of these activities is expected during a brain state that corresponds to locomotor quiescence. However, we discovered spontaneous motor-unrelated activity in a cluster of neurons in the anterior lateral ganglia. These comprise the cell types ASK, AFD, ADF, AWA, AWB, AWC, and ASH, all of which are sensory neurons. Except for ASK and AWC (see below), the exact cell types of these neurons were ambiguous in individual recordings. Therefore, we performed a global activity analysis as above but restricted to the spontaneously active neurons in this location: these spontaneous sensory neuron activities were also downregulated during quiescence (Figure 4B), showing that the quiescent brain state affects both the motor and sensory domains.

Next, we focused our analysis on the identifiable neuronal classes: most neuronal types that participated in population dynamics were downregulated during quiescence (Figure 4C). Remarkably, exceptions were GABAergic neuronal classes, notably the known sleep-promoting GABAergic and peptidergic neuron RIS (Turek et al., 2013, 2016), as well as the GABAergic head motor neuron class RME (composed of RMEL, RMER, RMEV, and RMED); these neurons retained stable Ca^{2+}-plateaus during quiescence. Moreover, the GABA uptake neuron AVF (Gendrel et al., 2016) and the GABA-and peptidergic interneuron class ALA (Gendrel et al., 2016) also remained active (Figures 4C and S4B). Spontaneously active sensory neurons were differentially affected, with some sensory neuron types downregulated during quiescence (ASK, Figure 4C) while others retained their activity (AWC, Figure 4C). Therefore, brain activity during starvation quiescence does not simply reflect absence of behavior-related activity but exhibits a specific neuronal signature.

Our recent work showed that neuronal population dynamics in *C. elegans* can be visualized using principal component analysis

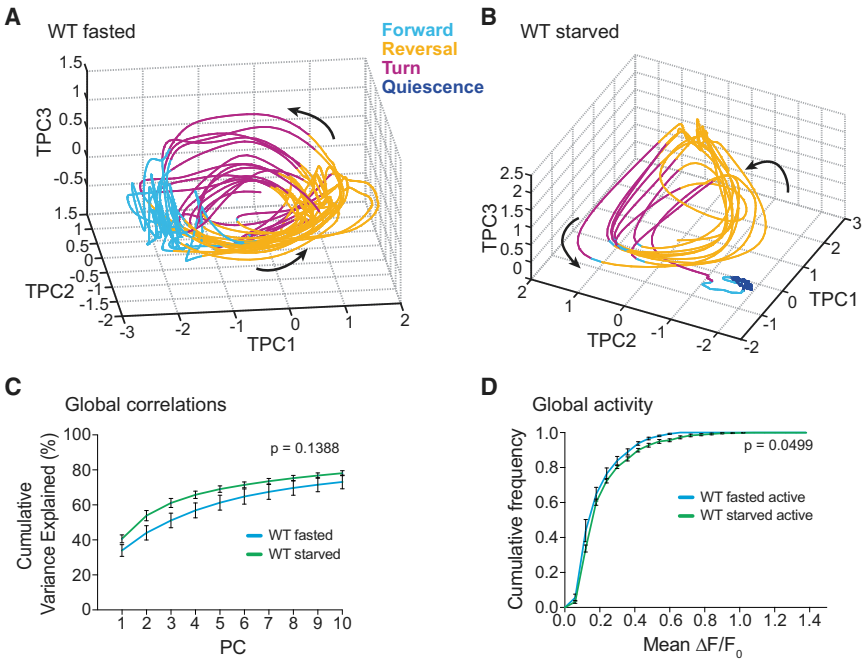

Figure 5. Neural Population Dynamics Are Robust to Starvation

(A and B) Phase plots of first three temporal principal components (TPCs) for the WT fasted (A) and WT starved (B) datasets shown in Figures 3B and 3C. Coloring indicates the respective motor command state, and arrows indicate the direction of time. More examples are shown in Figures S4A and S4B.

(C) Mean (±SEM) cumulative variance explained by first ten PCs during active brain state episodes.

(D) Mean (±SEM) cumulative fractional distributions of mean $\Delta F/F_0$ values across all detected neurons (excluding O_2-responsive neurons) during active brain state episodes. The p values in (C) and (D) indicate the probability of obtaining an equal or higher difference between the distributions after random shuffling; see Experimental Procedures. Number of recordings (n) = 6 each.

See also Figure S4 and Movie S2.

(PCA) as a dimensionality reduction method. PCA phase plots highlight the recurrent feature of brain dynamics, i.e., the brain state evolves through a stereotypic and repeating pattern of fluctuating but highly coordinated network activity. These dynamics correspond to a motor command sequence: forward crawling–reversal–dorsal or ventral turn (Kato et al., 2015) (Figures 5A and S4A). In contrast to the dynamic awake brain, the quiescent brain manifested as stationary fixed points in PCA space, occupying positions separable from the active brain (Figures 5B and S4B; Movie S2). Notably, this fixed-point attractor was not merely around zero in PCA space but received contributions from the above-described stable GABA neuron activity. Importantly, these features of starvation quiescence fully recapitulated the recently described characteristics of lethargus sleep (Cho and Sternberg, 2014; Nichols et al., 2017), further supporting our conclusion that starvation quiescence is a *C. elegans* sleep state.

Neuronal Population Dynamics Are Robust to Starvation

We next addressed the question how starvation affects brain-wide neuronal activity during awake periods. We hypothesized that neuronal population dynamics should be compromised upon severe starvation, e.g., by reducing signal amplitudes or by reducing the number of neurons recruited to the brain cycle, since both strategies could potentially reduce energy expenditure (Gleichmann and Mattson, 2011). Unexpectedly, a first inspection of our data indicated that the same behavior-related neuronal population dynamics as previously reported for well-fed worms were present irrespective of feeding state (Figures 3B and 3C). We next quantified these observations. A typical feature of neuronal population dynamics are brain-wide correlations, which can be quantified by PCA (Kato et al., 2015). We found that starvation did not alter the principal components (PCs) spectrum obtained from brain activity, showing that most dominant correlations remained intact (Figure 5C). We next set out to quantify global activity levels to test the hypothesis that starvation could alter neuronal signal amplitudes. We calculated the cumulative distributions of mean $\Delta F/F_0$ values for all neurons in each dataset exclusively during active (i.e., non-quiescent) brain episodes, exempting induced activity of O_2-sensory neurons. We found that starvation did not result in a general downregulation of neural activity during active episodes, but instead even subtly upregulated brain activity (Figure 5D). To our surprise, only a few of the identified neurons were regulated by starvation: RMED head motor neurons showed decreased activity, while a set of four anterior ganglion neurons with ambiguous identity (likely URA neurons) showed elevated activity upon starvation (Figures S6A–S6C). Furthermore, in WT fasted animals, neural activity of the sleep-promoting RIS interneuron (Turek et al., 2013, 2016) was bi-modally distributed among awake forward/turn command episodes, i.e., RIS can be found either active or inactive. Starvation shifted this distribution toward increased activity, showing that RIS is found mostly active during awake forward/turn command episodes upon starvation (Figure S6D). We recently reported such a shift in RIS activity levels comparing prelethargus animals with sleep-prone lethargus animals (Nichols et al., 2017). This finding in starved animals supports our previous interpretation that RIS activity levels during wakefulness indicate sleep pressure.

In conclusion, we made the surprising observation that starvation and thus decline in energy supply does not compromise awake brain activity but rather increases the amount of sleep.

DAF-2 Signaling Is Required to Maintain Neuronal Population Dynamics during Fasting

Neuronal population dynamics in fasted *daf-2* animals exhibited the same global features as the ones observed in starved WT animals (Figures 6A, 6B, and S4C). At the single-neuron level, *daf-2*

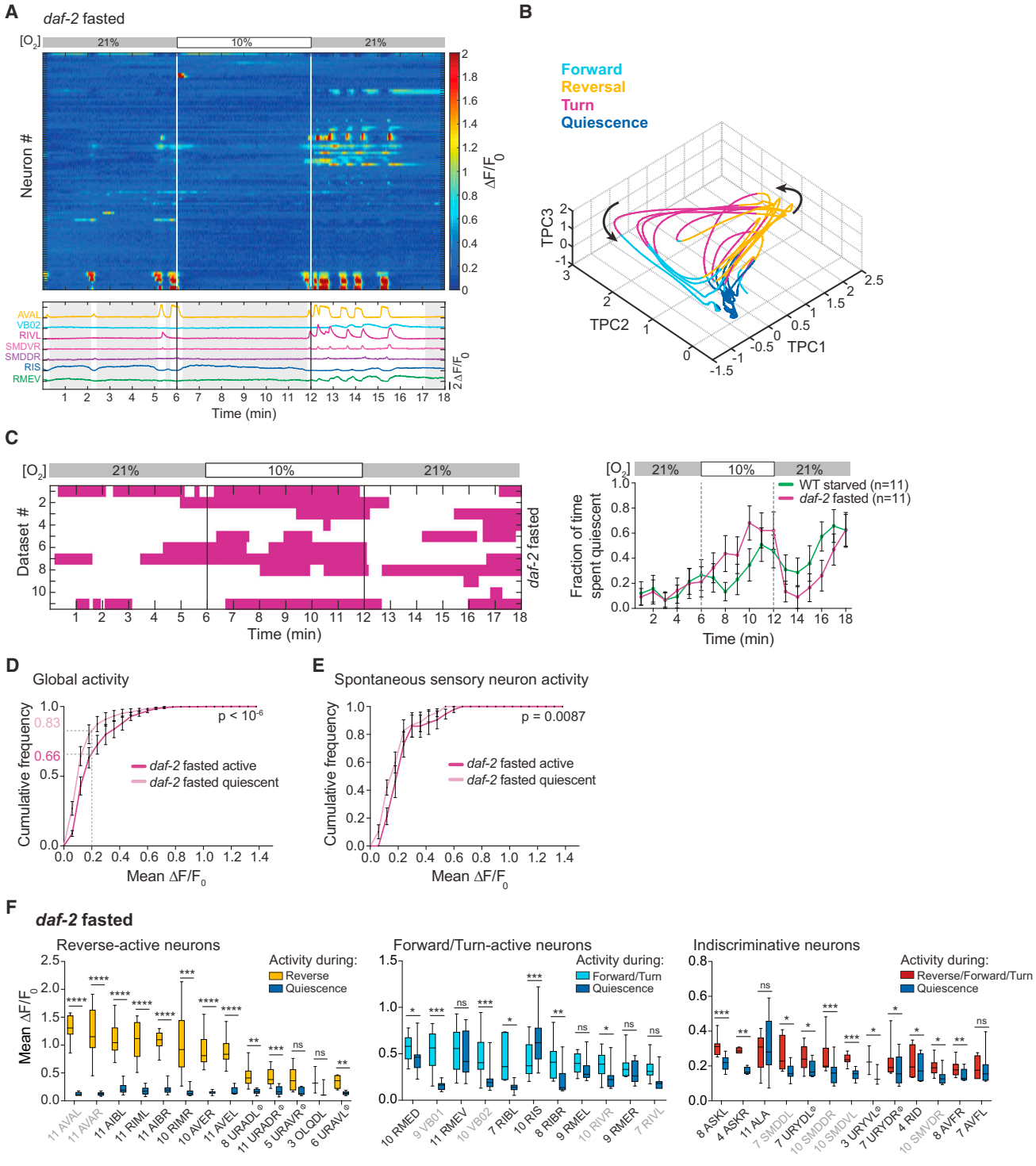

Figure 6. Signaling via DAF-2 Maintains Neural Population Dynamics during Fasting

(A) Top: heat plot of NLS-GCaMP5K fluorescence time series ($\Delta F/F_0$) and example traces (as in Figures 3B and 3C) of a single representative brain-wide imaging recording of a *daf-2* fasted worm. O_2 stimulation as indicated.

(B) Phase plot of first three temporal principal components (TPCs) for the dataset shown in (A). Coloring indicates the respective motor command state, and arrows indicate the direction of time. More examples can be found in Figure S4C.

(C) Left: brain state ethogram of quiescence episodes exhibited by *daf-2* fasted worms in brain-wide imaging recordings. One row corresponds to one recording, each a different animal. Right: traces show mean (±SEM) fraction of time spent quiescent in 1-min bins. n indicates number of recordings. WT starved control (green trace) shows same data as in Figure 3D.

(legend continued on next page)

fasted animals did not show modulation of the neurons tentatively identified as URAs, indicating that the *daf-2* genetic background did not generically recapitulate all effects of starvation on neuronal activity (Figure S6A). Consistent with our behavioral results, the frequency of quiescence episodes in *daf-2* fasted animals corresponded to a profile of WT starved animals. Moreover, unlike WT animals under imaging conditions, suppression of quiescence frequency and upregulation of reversal motor commands by O_2 upshift could be recapitulated in *daf-2* animals (Figures 6C and S5). *Daf-2* mutants are known for their resistance against stressors (e.g., Honda and Honda, 1999; Murakami and Johnson, 1996), suggesting them to be more resilient to the conditions of imaging and immobilization. As described above for WT starved worms, global neural activity as well the contribution from spontaneous sensory neuron activity was downregulated during quiescence in *daf-2* fasted animals; the latter however to a lesser extent (Figures 6D and 6E). The neural sleep signature that was observed in WT starved animals at the level of single neurons was also reiterated in *daf-2* fasted animals (Figure 6F), leading to a fixed point in PCA space (Figure 6B). The distribution of RIS activity levels appeared intermediate between WT fasted and starved animals, suggesting that insulin signaling potentially also affects RIS activity (Figure S6D).

In summary, the maintenance of brain-wide arousal during the initial fasting period requires signaling via the insulin receptor DAF-2.

Starvation and Mutation in *daf-2* Modulate the Activity of Sensory Neurons

Our behavioral genetics results suggested that feeding state and *daf-2* could modulate behavior at the level of sensory neurons. We found that O_2 downshift-evoked responses in BAG neurons (Zimmer et al., 2009) were unaffected by starvation or mutation in *daf-2* (Figures 7A and 7B). In contrast, O_2 upshift-evoked responses in URX neurons (Zimmer et al., 2009), in particular the sustained response component (Busch et al., 2012), were increased by starvation. Mutation in *daf-2* had the opposite effect on URX sensory responses, leading to attenuation (Figures 7C, 7D, and S7).

Recent studies reported *daf-2* requirement for evoked activity in some of the lateral ganglion sensory neurons (Leinwand and Chalasani, 2013; Leinwand et al., 2015). We thus tested whether *daf-2* could affect their spontaneous activity. Based on its stereotypic position, we could unambiguously identify the chemosensory neuron class ASK across multiple datasets. ASK exhibited spontaneous calcium spiking activity (Figure 7E). We found that quiescence suppressed ASK peak amplitudes in both WT starved and *daf-2* fasted animals as compared to active periods (Figure 7F). Furthermore, ASK activity during active periods was lower in *daf-2* fasted than in both WT fasted and starved animals (Figures 7F and S6C).

In summary, ASK and URX neurons provide additional (Leinwand et al., 2015; Leinwand and Chalasani, 2013) examples of neurons that are subject to modulation by *daf-2*, suggesting that regulation of sensory neuron activity is one major mode of DAF-2 action.

DISCUSSION

Insulin Signaling as an Arousal Pathway to Balance Energy Availability and Expenditure

We characterize here an adaptive behavioral strategy that is regulated in dependence of energy availability. Short periods of food deprivation upregulate a behavioral response to the putatively food-indicating cue O_2 (Gray et al., 2004; Hums et al., 2016). Our observations are paralleled by several other studies in *C. elegans* and fruit flies in which acute food deprivation modulates sensory responsiveness, either positively or negatively (Bräcker et al., 2013; Chao et al., 2004; Ezcurra et al., 2011; Ghosh et al., 2016). We hence propose that this transient state of arousal functions to enable active food search when external food sources decline but internal energy supply is still replete. While insulin signaling in *C. elegans* is mostly known for its critical role in regulating life span, metabolism, and reproductive development (for review, see Murphy and Hu, 2013), we show here that it also functions as a regulator of sleep and wakefulness. Neuronal insulin signaling might act as a measure of internal energy resources to maintain the arousal state as long as internal energy supply permits high locomotor activity. In this model, prolonged food deprivation leads to a gradual decline of insulin levels that causes the arousing effect of DAF-2 signaling to diminish and leads to upregulation of *daf-16*-dependent sleep. Importantly, a *daf-16;daf-2* double mutant continues to display reduced sleep levels, suggesting the involvement of other pathways converging onto DAF-16 to be involved in the regulation of sleep upon starvation.

We furthermore describe head-waving as an additional starvation-dependent behavior. While head-waving behavior likely serves other yet-to-be-identified functions, in the present study we show that it often precedes the transition into sleep episodes. In our previous work, we showed that the transition probability to enter lethargus sleep was a function of forward command state duration (Nichols et al., 2017). In analogy, we interpret head-waving as a state of reduced arousal, thereby increasing the probability to transit into starvation sleep. Consistent with this interpretation, the broadly sensory-deficient *osm-9* mutants

(D) Mean (±SEM) cumulative fractional distributions of mean $\Delta F/F_0$ values across all neurons (excluding O_2-responsive neurons) during active or quiescent episodes, in *daf-2* fasted animals. Dashed gray lines denote inactivity cutoff, below which neurons were usually found inactive. Number of recordings (n) = 6.
(E) Mean (±SEM) cumulative fractional distributions of mean $\Delta F/F_0$ values across spontaneously active sensory neurons during active or quiescent episodes. Number of recordings (n) = 6.
(F) Mean $\Delta F/F_0$ of identified neurons during each neuron's principal active state (reverse, forward, or active irrespective of motor state) and the quiescent state in *daf-2* fasted recordings. Boxplots show median, interquartile range, and min to max whiskers. Labels indicate putative neuron IDs. Ambiguous IDs are denoted with Φ (see Experimental Procedures for alternatives). Number of data points for each neuron (n) indicated. Grayed neuronal classes were used for classification of quiescent brain states. Paired t tests (****$p < 0.0001$, ***$p \leq 0.001$, **$p \leq 0.01$, *$p \leq 0.05$; ns, $p > 0.05$).
The p values in (D) and (E) indicate the probability of obtaining an equal or higher difference between the distributions after random shuffling of quiescence episodes; see Experimental Procedures. See also Figures S4–S6.

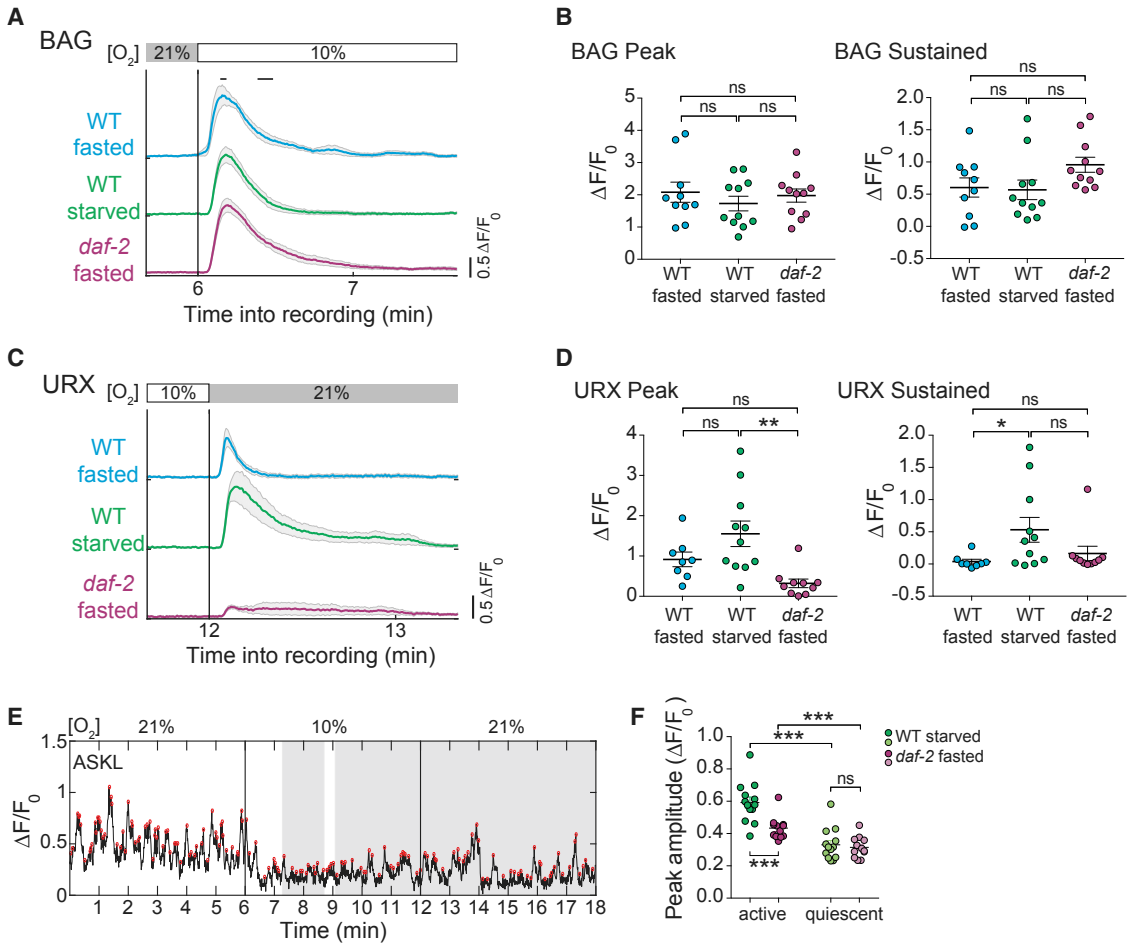

Figure 7. Starvation and Mutation in *daf-2* Modulate the Activity of Sensory Neurons

(A–D) Traces show means (±SEM) $\Delta F/F_0$ of O_2-downshift-sensing BAG neurons (A) and O_2-upshift-sensing URX neurons (C), respectively, extracted from brain-wide imaging recordings. Scatter bar plots (mean ± SEM) of peak (left) and sustained (right) BAG (B) and URX (D) activity. Bars in (A) indicate time periods used for BAG measurements; Figure S7 shows time periods for URX quantification. Number of measured neurons (n): 8-11. Significance of BAG was determined using one-way ANOVA with Sidak's correction (ns, $p > 0.05$), and of URX using Kruskal-Wallis test with Dunn's correction (**$p = 0.0016$, *$p = 0.0297$; ns, $p > 0.05$).

(E) Exemplary Ca^{2+} activity trace of an ASK neuron from the dataset shown in Figure 3C. Gray shadings indicate quiescent brain state episodes. Red circles indicate detected peaks.

(F) Scatter bar plots (mean ± SEM) of mean peak amplitude of ASK activity during active and quiescent periods. Comparisons within one genotype were done using Wilcoxon matched-pairs signed-rank test; comparisons in-between genotypes were made using Mann-Whitney test (***$p \leq 0.001$; ns, $p > 0.9999$). Number of detected ASK neurons for analysis (n): WT starved, n = 13; *daf-2* fasted, n = 12.

See also Figure S7.

failed to enter the head-waving state, leading to largely reduced quiescence levels. These data also suggest that head-waving is triggered by yet-to-be-identified *osm-9*-dependent O_2 sensors and/or other sensory neurons.

In summary, we propose that starvation-induced sleep in worms is a reversible adaptive behavior to conserve energy.

Neuronal Mechanisms Linking Energy State and the Control of Sleep

Recent work described the sleep-promoting RIS interneuron (Turek et al., 2013, 2016) and arousing O_2-sensory circuits as antagonistic regulators of sleep-wake transitions during lethargus (Nichols et al., 2017). In the present study, we show that increased sleep drive upon starvation was likewise associated with elevated RIS activity levels. Remarkably, in fasted *daf-2* animals, which recapitulated many features of starved WT animals, the distribution of RIS activity levels during active brain states was only slightly shifted toward increased activity. This suggests that DAF-2-dependent as well DAF-2-independent mechanisms must contribute to the observed starvation-dependent RIS modulation in WT animals. *Daf-2* and *daf-16* are expressed broadly, with highest expression levels in most of the aforementioned lateral ganglion sensory neurons (Cao et al., 2017). This is consistent with our rescue experiments using the *Posm-9* driver, which is prominently expressed in this sensory neuron cluster (Colbert et al., 1997). In accordance with recent work (Leinwand et al., 2015; Leinwand and Chalasani, 2013), we show that *daf-2* promotes spontaneous and

evoked activity in sensory neurons. This indicates that the absence of *daf-2* signaling increases arousal thresholds sufficiently to promote sleep without elevated RIS activity. However, broad deficiency in sensory neuron signaling like in *osm-9* mutants reduced quiescence, likely because the permissive head-waving state is triggered by still-unknown sensory neurons.

The *C. elegans* genome contains 40 genes for insulin-like ligands (Hobert, 2013; Pierce et al., 2001); therefore, the relevant DAF-2 ligands mediating the arousal state and their tissue expressions remain to be identified. Various individual insulin-like peptides interact in complex signaling networks, resulting in differential effects on biological functions (Fernandes de Abreu et al., 2014). We speculate that starvation results in the downregulation of a specific set of insulin ligands. A loss-of-function mutation in *daf-2* thus presents an extreme manifestation of insulin signaling disruption. Moreover, insulin signaling interacts with other hormonal signaling pathways in worms (Murphy and Hu, 2013). Both could explain why *daf-2* animals do not fully phenocopy starved animals.

Sleep as an Adaptive Strategy to Manage Energy-Expensive Neuronal Signaling

Neural signaling, in particular synaptic transmission, is known to be energy-demanding (Howarth et al., 2012; Rangaraju et al., 2014), yet whether there are specific mechanisms in place that help sustain neuronal signaling in the face of energy scarcity was largely unknown. *C. elegans* neurons lack classic action potentials (Goodman et al., 1998); however, these account for only 15%–22% of the neuronal energy budget in vertebrates. The remainder is allocated to other neuronal signaling mechanisms (Howarth et al., 2012), which are conserved between *C. elegans* and vertebrates (Hobert, 2013), suggesting a similarly high energetic cost of neuronal signaling in worms. We show that neuronal population dynamics, which involve the coordinated activity of a high fraction of all neurons, are largely robust to severe starvation. Our work thus points to a critical importance of these dynamics as they are maintained despite a presumably high energetic cost. Importantly, neuronal population dynamics have been described in several animal species ranging from invertebrates to primates (e.g., Briggman et al., 2005; Bruno et al., 2015; Churchland et al., 2012). We describe that, in worms, the major effect of starvation on brain activity is the frequent and reversible transition into a sleep brain state. Our results suggest that similar adaptation strategies might be applied by larger animals to maintain neuronal network function.

Recent studies reported a cellular mechanism by which *C. elegans* maintains its neural signaling capacity upon energy stress, via synaptic recruitment of metabolic enzymes (Jang et al., 2016). Here, we suggest an additional systemic network-level mechanism. Instead of compromising the dynamic properties of its neuronal networks during active processing, starvation introduces intermittent sleep episodes, during which neuronal activities are systemically downregulated. This downregulation of neuronal signaling in combination with lack of muscle activity thereby potentially allow a reduction in energy consumption.

EXPERIMENTAL PROCEDURES

Further details on all procedures and a comprehensive list of worm strains can be found in Supplemental Experimental Procedures.

Worm Population Behavioral Recordings

The experiments were performed at 20°C, as described previously (Hums et al., 2016; Zimmer et al., 2009). In brief, 1-day-old adult hermaphrodites were transferred to a 56 × 56-mm recording region on bacteria-free nematode growth medium (NGM) agar assay plates. Recordings were acquired at 3 Hz on a 4- to 5-megapixel charge-coupled device (CCD) camera. For starved assays, animals were food-deprived on NGM agar for 16 hr. Temperature-sensitive *daf-2(e1370)* mutants, *daf-2* rescue strains, and corresponding controls were maintained at permissive 16°C and shifted to restrictive 25°C in the evening before the experiment approximately 7 hr before starvation was initiated.

Video Tracking of Animal Behavior and Behavioral State Identification

Tracking and analysis were performed using customized MATLAB scripts that are based on the Parallel Worm Tracker, as described previously (Ramot et al., 2008). We distinguish three behavioral states: an active state, during which the worm is moving; a quiescent state when the worm is completely still; and head-waving, which is characterized by retained dorso-ventral movement of the head/neck region. The states were determined in 1-s bins on the basis of threshold values of speed and instantaneous changes in object eccentricity (see also Figure S1C).

Brain-wide Ca^{2+} Imaging in Microfluidic Device

Animals were immobilized with 1 mM tetramisole in NGM buffer in microfluidic devices that allow controlled O_2 stimuli delivery as previously described (Schrödel et al., 2013). Data were acquired using an inverted spinning disk microscope (UltraViewVoX; PerkinElmer) with an electron-multiplying charge-coupled device (EMCCD) camera (C9100-13; Hamamatsu) at 1.6–2.6 volumes per second.

Statistics

Standard statistical tests were performed in GraphPad Prism 7; all resampling tests were performed using custom scripts in MATLAB. Details on choice and implementation of each statistical test, post-test as well as sample size, displayed data, and p values can be found with each figure legend and Supplemental Experimental Procedures.

SUPPLEMENTAL INFORMATION

Supplemental Information includes Supplemental Experimental Procedures, seven figures, one table, and two movies and can be found with this article online at https://doi.org/10.1016/j.celrep.2017.12.091.

ACKNOWLEDGMENTS

We thank Harris Kaplan and Mara Andrione for critical reading of the manuscript, Richard Latham for generating genetic RMG ablation strains, the National Bioresource Project (NBRP) and *Caenorhabditis* Genetics Center (NIH Office of Research Infrastructure Programs, P40 OD010440) for knockout strains, and the Bargmann, Iino, Zhen, and Mano laboratories for strains and reagents. The research leading to these results has received funding from the European Community's Seventh Framework Programme (FP7/2007-2013)/ERC (grant agreement 281869) and the Research Institute of Molecular Pathology (IMP). M.Z. is supported by the Simons Foundation (grant 324958). The IMP is funded by Boehringer Ingelheim.

AUTHOR CONTRIBUTIONS

S.S. designed and performed experiments, developed analytical methods, and analyzed data. F.M. performed *daf-2* rescue experiments and analyzed

data. M.Z. designed experiments, developed analytical methods, and led the project. S.S. and M.Z. wrote the manuscript.

DECLARATION OF INTERESTS

The authors declare no competing interests.

Received: July 5, 2017
Revised: November 16, 2017
Accepted: December 23, 2017
Published: January 23, 2018

REFERENCES

Alvarenga, T.A.F., Andersen, M.L., Papale, L.A., Antunes, I.B., and Tufik, S. (2005). Influence of long-term food restriction on sleep pattern in male rats. Brain Res. *1057*, 49–56.

Bräcker, L.B., Siju, K.P., Varela, N., Aso, Y., Zhang, M., Hein, I., Vasconcelos, M.L., and Grunwald Kadow, I.C. (2013). Essential role of the mushroom body in context-dependent CO_2 avoidance in *Drosophila*. Curr. Biol. *23*, 1228–1234.

Briggman, K.L., Abarbanel, H.D.I., and Kristan, W.B., Jr. (2005). Optical imaging of neuronal populations during decision-making. Science *307*, 896–901.

Bruno, A.M., Frost, W.N., and Humphries, M.D. (2015). Modular deconstruction reveals the dynamical and physical building blocks of a locomotion motor program. Neuron *86*, 304–318.

Busch, K.E., Laurent, P., Soltesz, Z., Murphy, R.J., Faivre, O., Hedwig, B., Thomas, M., Smith, H.L., and de Bono, M. (2012). Tonic signaling from O_2 sensors sets neural circuit activity and behavioral state. Nat. Neurosci. *15*, 581–591.

Cao, J., Packer, J.S., Ramani, V., Cusanovich, D.A., Huynh, C., Daza, R., Qiu, X., Lee, C., Furlan, S.N., Steemers, F.J., et al. (2017). Comprehensive single-cell transcriptional profiling of a multicellular organism. Science *357*, 661–667.

Chao, M.Y., Komatsu, H., Fukuto, H.S., Dionne, H.M., and Hart, A.C. (2004). Feeding status and serotonin rapidly and reversibly modulate a *Caenorhabditis elegans* chemosensory circuit. Proc. Natl. Acad. Sci. USA *101*, 15512–15517.

Cho, J.Y., and Sternberg, P.W. (2014). Multilevel modulation of a sensory motor circuit during *C. elegans* sleep and arousal. Cell *156*, 249–260.

Choi, S., Taylor, K.P., Chatzigeorgiou, M., Hu, Z., Schafer, W.R., and Kaplan, J.M. (2015). Sensory neurons arouse *C. elegans* locomotion via both glutamate and neuropeptide release. PLoS Genet. *11*, e1005359.

Churchland, M.M., Cunningham, J.P., Kaufman, M.T., Foster, J.D., Nuyujukian, P., Ryu, S.I., and Shenoy, K.V. (2012). Neural population dynamics during reaching. Nature *487*, 51–56.

Colbert, H.A., Smith, T.L., and Bargmann, C.I. (1997). OSM-9, a novel protein with structural similarity to channels, is required for olfaction, mechanosensation, and olfactory adaptation in *Caenorhabditis elegans*. J. Neurosci. *17*, 8259–8269.

Dillon, J., Holden-Dye, L., O'Connor, V., and Hopper, N.A. (2016). Context-dependent regulation of feeding behaviour by the insulin receptor, DAF-2, in *Caenorhabditis elegans*. Invert. Neurosci. *16*, 4.

Dwyer, D.S., and Aamodt, E.J. (2013). Insulin/IGF-1 signaling, including class II/III PI3Ks, β-arrestin and SGK-1, is required in *C. elegans* to maintain pharyngeal muscle performance during starvation. PLoS One *8*, e63851.

Ezcurra, M., Tanizawa, Y., Swoboda, P., and Schafer, W.R. (2011). Food sensitizes *C. elegans* avoidance behaviours through acute dopamine signalling. EMBO J. *30*, 1110–1122.

Fernandes de Abreu, D.A., Caballero, A., Fardel, P., Stroustrup, N., Chen, Z., Lee, K., Keyes, W.D., Nash, Z.M., López-Moyado, I.F., Vaggi, F., et al. (2014). An insulin-to-insulin regulatory network orchestrates phenotypic specificity in development and physiology. PLoS Genet. *10*, e1004225.

Frézal, L., and Félix, M.-A. (2015). *C. elegans* outside the Petri dish. eLife *4*, e05849.

Gallagher, T., Bjorness, T., Greene, R., You, Y.-J., and Avery, L. (2013). The geometry of locomotive behavioral states in *C. elegans*. PLoS One *8*, e59865.

Gems, D., Sutton, A.J., Sundermeyer, M.L., Albert, P.S., King, K.V., Edgley, M.L., Larsen, P.L., and Riddle, D.L. (1998). Two pleiotropic classes of daf-2 mutation affect larval arrest, adult behavior, reproduction and longevity in *Caenorhabditis elegans*. Genetics *150*, 129–155.

Gendrel, M., Atlas, E.G., and Hobert, O. (2016). A cellular and regulatory map of the GABAergic nervous system of *C. elegans*. eLife *5*, e17686.

Ghosh, R., and Emmons, S.W. (2008). Episodic swimming behavior in the nematode *C. elegans*. J. Exp. Biol. *211*, 3703–3711.

Ghosh, D.D., Sanders, T., Hong, S., McCurdy, L.Y., Chase, D.L., Cohen, N., Koelle, M.R., and Nitabach, M.N. (2016). Neural architecture of hunger-dependent multisensory decision making in *C. elegans*. Neuron *92*, 1049–1062.

Gleichmann, M., and Mattson, M.P. (2011). Neuronal calcium homeostasis and dysregulation. Antioxid. Redox Signal. *14*, 1261–1273.

Goodman, M.B., Hall, D.H., Avery, L., and Lockery, S.R. (1998). Active currents regulate sensitivity and dynamic range in *C. elegans* neurons. Neuron *20*, 763–772.

Gray, J.M., Karow, D.S., Lu, H., Chang, A.J., Chang, J.S., Ellis, R.E., Marletta, M.A., and Bargmann, C.I. (2004). Oxygen sensation and social feeding mediated by a *C. elegans* guanylate cyclase homologue. Nature *430*, 317–322.

Hill, A.J., Mansfield, R., Lopez, J.M.N.G., Raizen, D.M., and Van Buskirk, C. (2014). Cellular stress induces a protective sleep-like state in *C. elegans*. Curr. Biol. *24*, 2399–2405.

Hobert, O. (2013). The neuronal genome of *Caenorhabditis elegans*. WormBook *2013*, 1–106.

Honda, Y., and Honda, S. (1999). The *daf-2* gene network for longevity regulates oxidative stress resistance and Mn-superoxide dismutase gene expression in *Caenorhabditis elegans*. FASEB J. *13*, 1385–1393.

Howarth, C., Gleeson, P., and Attwell, D. (2012). Updated energy budgets for neural computation in the neocortex and cerebellum. J. Cereb. Blood Flow Metab. *32*, 1222–1232.

Hums, I., Riedl, J., Mende, F., Kato, S., Kaplan, H.S., Latham, R., Sonntag, M., Traunmüller, L., and Zimmer, M. (2016). Regulation of two motor patterns enables the gradual adjustment of locomotion strategy in *Caenorhabditis elegans*. eLife *5*, e14116.

Iwanir, S., Tramm, N., Nagy, S., Wright, C., Ish, D., and Biron, D. (2013). The microarchitecture of *C. elegans* behavior during lethargus: homeostatic bout dynamics, a typical body posture, and regulation by a central neuron. Sleep (Basel) *36*, 385–395.

Jang, S., Nelson, J.C., Bend, E.G., Rodríguez-Laureano, L., Tueros, F.G., Cartagenova, L., Underwood, K., Jorgensen, E.M., and Colón-Ramos, D.A. (2016). Glycolytic enzymes localize to synapses under energy stress to support synaptic function. Neuron *90*, 278–291.

Kato, S., Kaplan, H.S., Schrödel, T., Skora, S., Lindsay, T.H., Yemini, E., Lockery, S., and Zimmer, M. (2015). Global brain dynamics embed the motor command sequence of *Caenorhabditis elegans*. Cell *163*, 656–669.

Keene, A.C., Duboué, E.R., McDonald, D.M., Dus, M., Suh, G.S.B., Waddell, S., and Blau, J. (2010). Clock and cycle limit starvation-induced sleep loss in *Drosophila*. Curr. Biol. *20*, 1209–1215.

Kimura, K.D., Tissenbaum, H.A., Liu, Y., and Ruvkun, G. (1997). daf-2, an insulin receptor-like gene that regulates longevity and diapause in *Caenorhabditis elegans*. Science *277*, 942–946.

Landauer, R. (1961). Irreversibility and heat generation in the computing process. IBM J. Res. Dev. *5*, 183–191.

Laughlin, S.B. (2001). Energy as a constraint on the coding and processing of sensory information. Curr. Opin. Neurobiol. *11*, 475–480.

Leinwand, S.G., and Chalasani, S.H. (2013). Neuropeptide signaling remodels chemosensory circuit composition in *Caenorhabditis elegans*. Nat. Neurosci. *16*, 1461–1467.

Leinwand, S.G., Yang, C.J., Bazopoulou, D., Chronis, N., Srinivasan, J., and Chalasani, S.H. (2015). Circuit mechanisms encoding odors and driving aging-associated behavioral declines in *Caenorhabditis elegans*. eLife *4*, e10181.

Longden, K.D., Muzzu, T., Cook, D.J., Schultz, S.R., and Krapp, H.G. (2014). Nutritional state modulates the neural processing of visual motion. Curr. Biol. *24*, 890–895.

Macosko, E.Z., Pokala, N., Feinberg, E.H., Chalasani, S.H., Butcher, R.A., Clardy, J., and Bargmann, C.I. (2009). A hub-and-spoke circuit drives pheromone attraction and social behaviour in *C. elegans*. Nature *458*, 1171–1175.

McCloskey, R.J., Fouad, A.D., Churgin, M.A., and Fang-Yen, C. (2017). Food responsiveness regulates episodic behavioral states in *Caenorhabditis elegans*. J. Neurophysiol. *117*, 1911–1934.

Mink, J.W., Blumenschine, R.J., and Adams, D.B. (1981). Ratio of central nervous system to body metabolism in vertebrates: its constancy and functional basis. Am. J. Physiol. *241*, R203–R212.

Murakami, S., and Johnson, T.E. (1996). A genetic pathway conferring life extension and resistance to UV stress in *Caenorhabditis elegans*. Genetics *143*, 1207–1218.

Murphy, C.T., and Hu, P.J. (2013). Insulin/insulin-like growth factor signaling in *C. elegans*. WormBook *2013*, 1–43.

Nichols, A.L.A., Eichler, T., Latham, R., and Zimmer, M. (2017). A global brain state underlies *C. elegans* sleep behavior. Science *356*, eaam6851.

Persson, A., Gross, E., Laurent, P., Busch, K.E., Bretes, H., and de Bono, M. (2009). Natural variation in a neural globin tunes oxygen sensing in wild *Caenorhabditis elegans*. Nature *458*, 1030–1033.

Pierce, S.B., Costa, M., Wisotzkey, R., Devadhar, S., Homburger, S.A., Buchman, A.R., Ferguson, K.C., Heller, J., Platt, D.M., Pasquinelli, A.A., et al. (2001). Regulation of DAF-2 receptor signaling by human insulin and ins-1, a member of the unusually large and diverse *C. elegans* insulin gene family. Genes Dev. *15*, 672–686.

Plaçais, P.-Y., and Preat, T. (2013). To favor survival under food shortage, the brain disables costly memory. Science *339*, 440–442.

Raizen, D.M., Lee, R.Y.N., and Avery, L. (1995). Interacting genes required for pharyngeal excitation by motor neuron MC in *Caenorhabditis elegans*. Genetics *141*, 1365–1382.

Raizen, D.M., Zimmerman, J.E., Maycock, M.H., Ta, U.D., You, Y.-J., Sundaram, M.V., and Pack, A.I. (2008). Lethargus is a *Caenorhabditis elegans* sleep-like state. Nature *451*, 569–572.

Ramot, D., Johnson, B.E., Berry, T.L., Jr., Carnell, L., and Goodman, M.B. (2008). The Parallel Worm Tracker: a platform for measuring average speed and drug-induced paralysis in nematodes. PLoS ONE *3*, e2208.

Rangaraju, V., Calloway, N., and Ryan, T.A. (2014). Activity-driven local ATP synthesis is required for synaptic function. Cell *156*, 825–835.

Schrödel, T., Prevedel, R., Aumayr, K., Zimmer, M., and Vaziri, A. (2013). Brain-wide 3D imaging of neuronal activity in *Caenorhabditis elegans* with sculpted light. Nat. Methods *10*, 1013–1020.

Sexstone, A.J., Revsbach, N.P., Parkin, T.B., and Tiedje, J.M. (1985). Direct measurement of oxygen profiles and denitrification rates in soil aggregates. Soil Sci. Soc. Am. J. *49*, 645–651.

Slocumb, M.E., Regalado, J.M., Yoshizawa, M., Neely, G.G., Masek, P., Gibbs, A.G., and Keene, A.C. (2015). Enhanced sleep is an evolutionarily adaptive response to starvation stress in *Drosophila*. PLoS One *10*, e0131275.

Sze, J.Y., Victor, M., Loer, C., Shi, Y., and Ruvkun, G. (2000). Food and metabolic signalling defects in a *Caenorhabditis elegans* serotonin-synthesis mutant. Nature *403*, 560–564.

Turek, M., Lewandrowski, I., and Bringmann, H. (2013). An AP2 transcription factor is required for a sleep-active neuron to induce sleep-like quiescence in *C. elegans*. Curr. Biol. *23*, 2215–2223.

Turek, M., Besseling, J., Spies, J.-P., König, S., and Bringmann, H. (2016). Sleep-active neuron specification and sleep induction require FLP-11 neuropeptides to systemically induce sleep. eLife *5*, e12499.

Waterson, M.J., and Horvath, T.L. (2015). Neuronal regulation of energy homeostasis: beyond the hypothalamus and feeding. Cell Metab. *22*, 962–970.

White, J.G., Southgate, E., Thomson, J.N., and Brenner, S. (1986). The structure of the nervous system of the nematode *Caenorhabditis elegans*. Philos. Trans. R. Soc. Lond. B Biol. Sci. *314*, 1–340.

Witham, E., Comunian, C., Ratanpal, H., Skora, S., Zimmer, M., and Srinivasan, S. (2016). *C. elegans* body cavity neurons are homeostatic sensors that integrate fluctuations in oxygen availability and internal nutrient reserves. Cell Rep. *14*, 1641–1654.

Zimmer, M., Gray, J.M., Pokala, N., Chang, A.J., Karow, D.S., Marletta, M.A., Hudson, M.L., Morton, D.B., Chronis, N., and Bargmann, C.I. (2009). Neurons detect increases and decreases in oxygen levels using distinct guanylate cyclases. Neuron *61*, 865–879.

Cell Reports, Volume *22*

Supplemental Information

Energy Scarcity Promotes a Brain-wide Sleep State Modulated by Insulin Signaling in *C. elegans*

Susanne Skora, Fanny Mende, and Manuel Zimmer

Supplemental information

This PDF contains:

Supplemental figures S1-S7
Supplemental figure legends
Supplemental table S1
Supplemental experimental procedures
Supplemental references

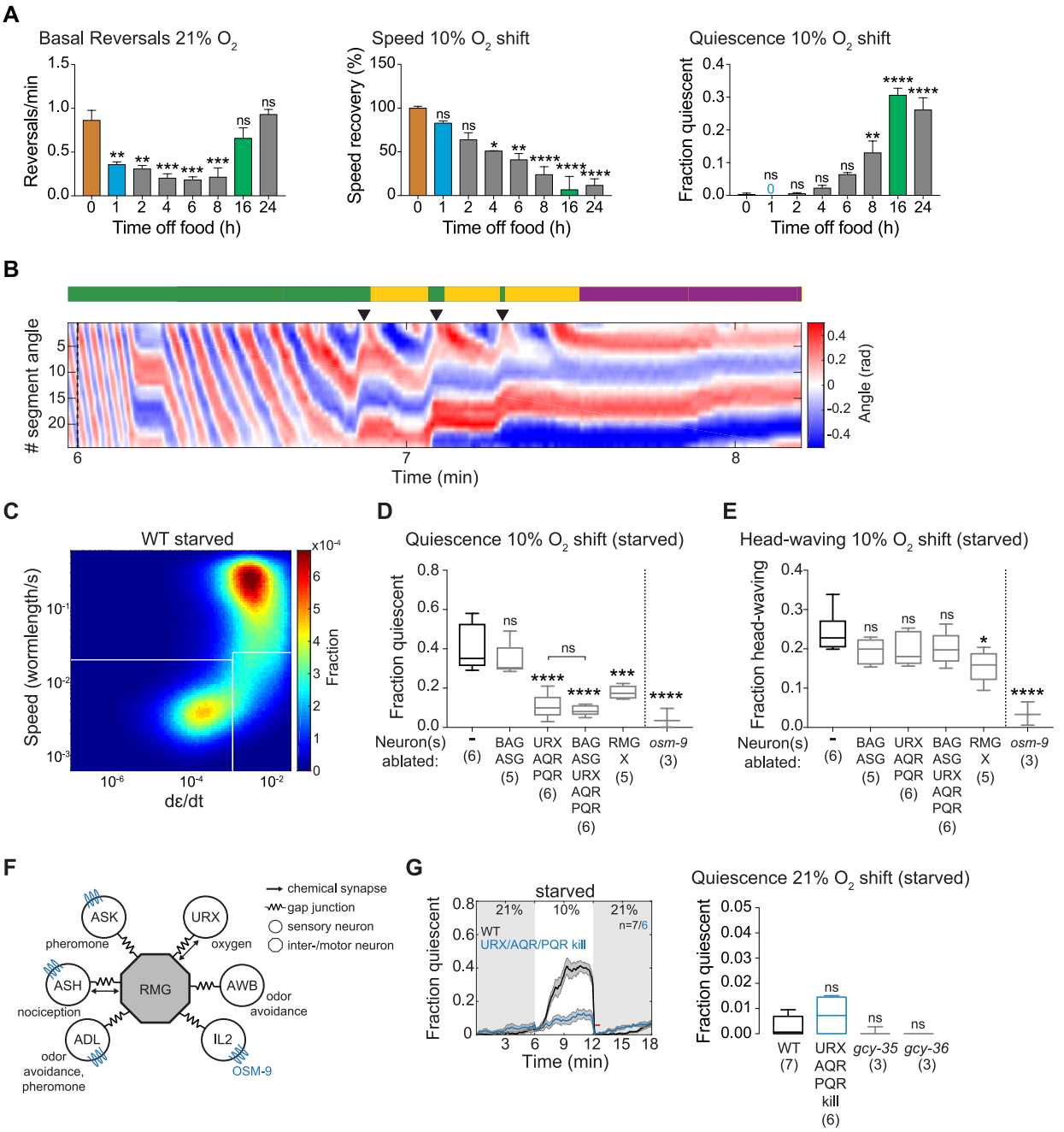

Figure S1. Food deprivation causes a gradual change in O_2-related behaviors and quiescence is under control of sensory circuits. Related to Figure 1.

(A) Quantification of basal reversal rate, speed recovery following O_2 downshift and O_2 downshift-induced quiescence, upon increasing time off food. Basal reversal rate was quantified during interval labelled with black bar in Figure 1A, speed recovery and quiescence as described for Figures 1B and 1C. 0 h off food indicates well-fed. Bars show mean ± SEM. Bar colors match colors in Figure 1. Time points were compared to the well-fed condition using one-way ANOVA with Dunnett's correction (**** $p < 0.0001$, *** $p \leq 0.001$, ** $p \leq 0.01$, * $p = 0.0106$, ns $p > 0.05$). Number of experiments (n) used: n = 3, except 8 h and 16 h time points for which n = 4 (~100 animals each).

(B) Body posture kymograph of 24 intersegment angles from head (1) to tail (24) for the worm shown in Movie S1. O_2 downshift starts at 6 min into the recording (dotted black line). Colored line above kymograph indicates behavioral state according to color scheme used in Figure 1G (green: active, yellow: head-waving, purple: quiescent). Black arrowheads indicate reversals.

(C) 2D fractional density distribution (log-log scale) of speed vs. derivative of eccentricity (dε/dt) of WT starved animals from all experiments of the type shown in Figure 1C (n=28) and the experiments shown in Figures 1E and 1F (n=4 each), including all O_2 concentration periods. White lines indicate the thresholds used to identify behavioral states (quiescent: < 0.00107 (dε/dt) and < 0.02 (speed); head-waving: > 0.00107 (dε/dt) and < 0.025 (speed)).

(D and E) Effect of neuronal ablations and sensory signaling-defective *osm-9* mutants on quiescence (**D**) and head-waving (**E**). Quantification intervals as in Figures 1C and 1D. The X denoted with RMG ablation strain signifies ablation of an additional unknown neuron, see note with methods. Boxplots display median, interquartile range and min to max whiskers. All strains were compared to WT and additional comparisons were made as indicated, using one-way ANOVA with Sidak's correction (**** $p < 0.0001$, *** $p = 0.0002$, * $p = 0.0112$, ns $p > 0.05$). Number of experiments (n) indicated below each genotype.
(F) Illustration of hub and spoke circuit diagram showing RMG and its gap junction sensory neuron partners. OSM-9-expressing neurons indicated in blue, according to Colbert et al., 1997.
(G) Left: Population means (± SEM) of fraction quiescent under O_2 stimulation as indicated for starved WT (black) and URX/AQR/PQR-ablated (blue) animals. Right: Quantification during period indicated by red bar in left panel. Quantification additionally shows animals deficient in the guanylate cyclases *gcy-35* and *gcy-36*, which are required for O_2 sensation. Significance against WT determined using one-way ANOVA with Dunnett's correction (ns $p > 0.05$). Boxplots show median, interquartile range and min to max whiskers. Number of experiments (n) indicated below each boxplot. Experiments of URX/AQR/PQR cell kill are the same as those in Figures S1D and S1E.

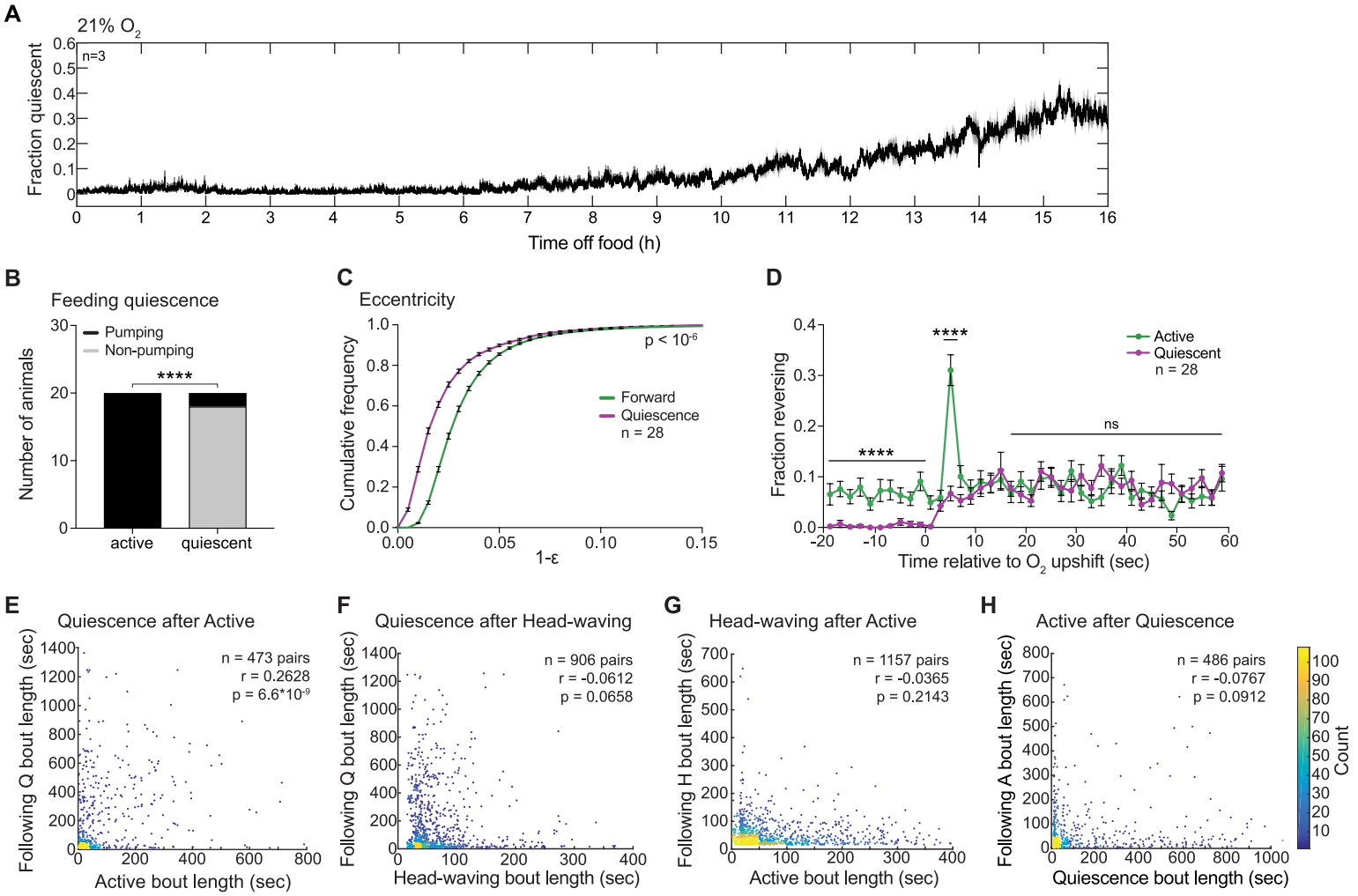

Figure S2. Starvation quiescence is a behavioral sleep-like state. Related to Figure 1.

(A) Population mean (± SEM) of fraction quiescent during long-term, undisturbed recording of WT worms at constant 21% O_2. Number of experiments (n) indicated (~100 animals each).

(B) Number of active and quiescent starved WT animals exhibiting pumping versus non-pumping behavior during a 60 sec observation period. Total number of pumps observed in quiescent worms = 3, also see methods. Number of animals (n) = 20 for each active and quiescent. Fisher's exact test (**** $p < 0.0001$).

(C) Mean (± SEM) cumulative fractional distributions of shape factor 1-eccentricity (ε) during fast forward movement (> 0.1 mm/sec) versus quiescence from O_2 shift experiments in WT starved animals as in Figure 1C. P-value indicates chance of obtaining an equal or larger difference between the distributions after random shuffling, see methods. Number of experiments (n) indicated.

(D) Mean (± SEM) fraction of WT starved animals reversing, both pre and post O_2 upshift. Animals have either been active (green) or quiescent (purple) for 2 min prior to O_2 upshift. Number of experiments (n) indicated. Significance calculated for the time intervals indicated with black lines, using Mann-Whitney test (**** $p < 0.0001$, ns $p = 0.1114$).

(E-H) Scatter plots of quiescence (Q) bout length versus preceding active (A) bout length **(E)**, quiescence (Q) bout length versus preceding head-waving bout length **(F)**, head-waving (H) bout length versus preceding active bout length **(G)**, and active (A) bout length versus preceding quiescence bout length **(H)**. Data are taken from experiments shown in Figure 1F at constant 10% O_2, also see methods. n = number of successive bout pairs. Axes are cropped to aid visualization. Color indicates density of data points according to color bar on the right. r = Spearman correlation coefficient. The p-values are approximated by random permutations.

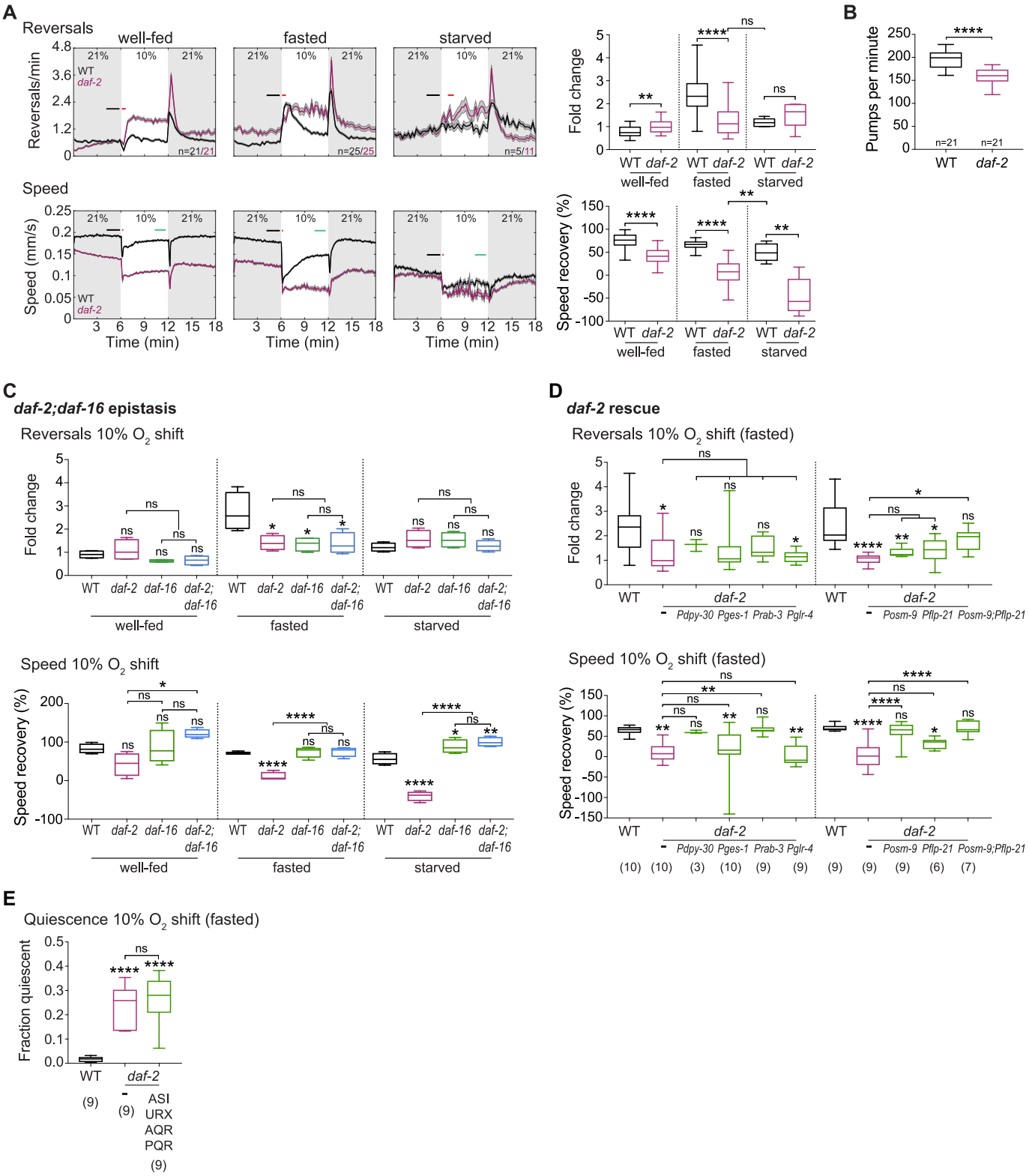
A
Reversals
well-fed
fasted
starved
Reversals/min
21%
10%
WT
daf-2
n=21/21
n=25/25
n=5/11
Speed
Speed (mm/s)
Time (min)
Fold change
Speed recovery (%)
WT daf-2
well-fed
fasted
starved
B
Pumps per minute
n=21
C
daf-2;daf-16 epistasis
Reversals 10% O2 shift
Speed 10% O2 shift
WT
daf-2
daf-16
daf-2; daf-16
D
daf-2 rescue
Reversals 10% O2 shift (fasted)
Speed 10% O2 shift (fasted)
Pdpy-30 Pges-1 Prab-3 Pglr-4
Posm-9 Pflp-21 Posm-9;Pflp-21
(10) (10) (3) (10) (9) (9) (9) (9) (9) (6) (7)
E
Quiescence 10% O2 shift (fasted)
Fraction quiescent
(9)
ASI
URX
AQR
PQR

Figure S3. The arousing effect of DAF-2 signaling is dependent on the FOXO transcription factor DAF-16. Related to Figure 2.

(A) Left: Population means (± SEM) of indicated behaviors with O_2 stimulation under indicated feeding states. n = number of experiments (40-120 animals each). Right: Quantifications using unpaired t-test (**** $p < 0.0001$, ** $p < 0.01$, ns $p > 0.05$). N-numbers as indicated on the left, except *daf-2* starved, where only experiments performed in parallel to WT were used for quantification (i.e. n = 5 for both WT and *daf-2* starved).

(B) Pharyngeal pumping rates of WT and *daf-2* animals in the presence of food. Number of worms (n) indicated. Unpaired t-test (**** $p < 0.0001$).

(C) Quantification of *daf-2; daf-16* epistasis experiment for O_2 downshift-dependent behaviors under indicated feeding states, using one-way ANOVA with Sidak's (reversals) or Tukey's (speed) correction (**** $p < 0.0001$, ** $p = 0.0063$, * $p < 0.05$, ns $p > 0.05$). Significance against WT is indicated above each boxplot. Additional comparisons as shown. Intervals quantified as shown in Figures 1A and 1B. Number of experiments (n) = 4 for each.

(D) Quantification of tissue-and cell-specific *daf-2* rescue experiments in fasted animals. *Pdpy-30*: ubiquitous, *Pges-1*: intestine, *Prab-3*: pan-neuronal, *Pglr-4*: inter- and motor neurons, *Posm-9*: sensory neurons, *Pflp-21*: RMG, FLP, ASJ, M2, URA, URX, ASI. Significance against WT is indicated above each boxplot. Additional comparisons as shown. One-way ANOVA with Sidak's correction (**** $p < 0.0001$, ** $p \leq 0.01$, * $p \leq 0.05$, ns $p > 0.05$). Number of experiments (n) indicated below each boxplot (~40 animals each).

(E) Quantification of rescue experiments in fasted animals driving *daf-2a* cDNA in ASI (using *Pgpa-4*) and URX, AQR, PQR (using *Pgcy-36*) neurons. Quantification interval as shown in Figure 1C. Significance against WT is indicated above each boxplot. One-way ANOVA with Sidak's correction (**** $p < 0.0001$, ns = 0.6338). Number of experiments (n) indicated below each boxplot (~40 animals each).

For all quantifications, boxplots show median, interquartile range and min to max whiskers.

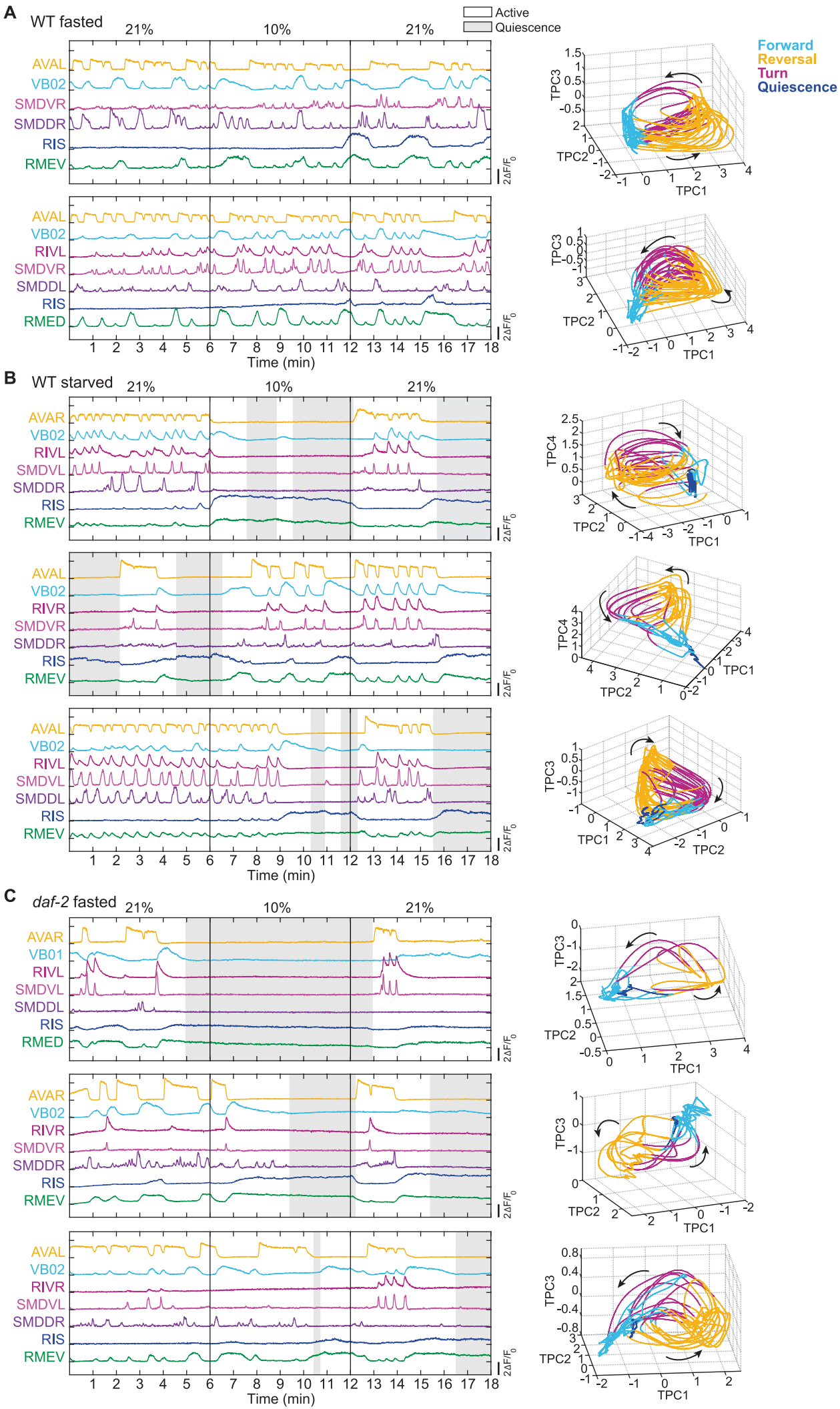
A
WT fasted
Active
Quiescence
21%
10%
21%
AVAL
VB02
SMDVR
SMDDR
RIS
RMEV
RIVL
SMDDL
RMED
2ΔF/F0
Time (min)
Forward
Reversal
Turn
Quiescence
TPC1
TPC2
TPC3
B
WT starved
AVAR
RIVR
SMDVL
RMEV
TPC4
C
daf-2 fasted

Figure S4. Starvation biases to intermittent neural sleep episodes while insulin signaling maintains continuous neural population dynamics during fasting. Related to Figures 3, 5 and 6.

Additional examples of brain-wide imaging recordings in WT fasted **(A)**, WT starved **(B)** and *daf-2* fasted **(C)** worms. Left: Traces show the activity of the reversal interneuron AVA, the forward motor neuron VB02/VB01, the turning motor neurons RIV, SMDV and SMDD, as well as the GABAergic neurons RIS and RMEV/D. O_2 concentration indicated. Grey shadings denote quiescence periods. Right: Phase plot of first 3 integrated principal components (TPCs). Note that for 2 WT starved datasets TPCs 1, 2 and 4 are shown (also see methods). Coloring indicates the respective motor command state and arrows indicate the direction of the trajectory.

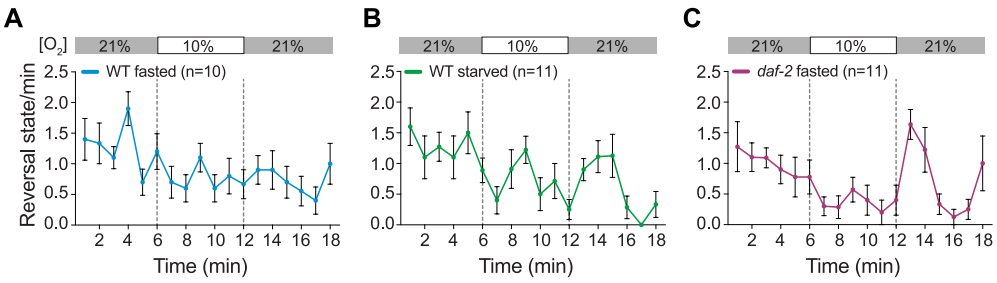

Figure S5. Behavioral regulation downstream of sensory processing is inefficient under imaging conditions in WT but not *daf-2* animals. Related to Figures 3 and 6.

Reversal command state in WT fasted **(A)**, WT starved **(B)** and *daf-2* fasted **(C)** brain-wide imaging recordings as read-out by the state of the reversal command interneuron AVA, quantified as mean (± SEM) AVA rise phases per minute. Number of recordings (n) indicated.

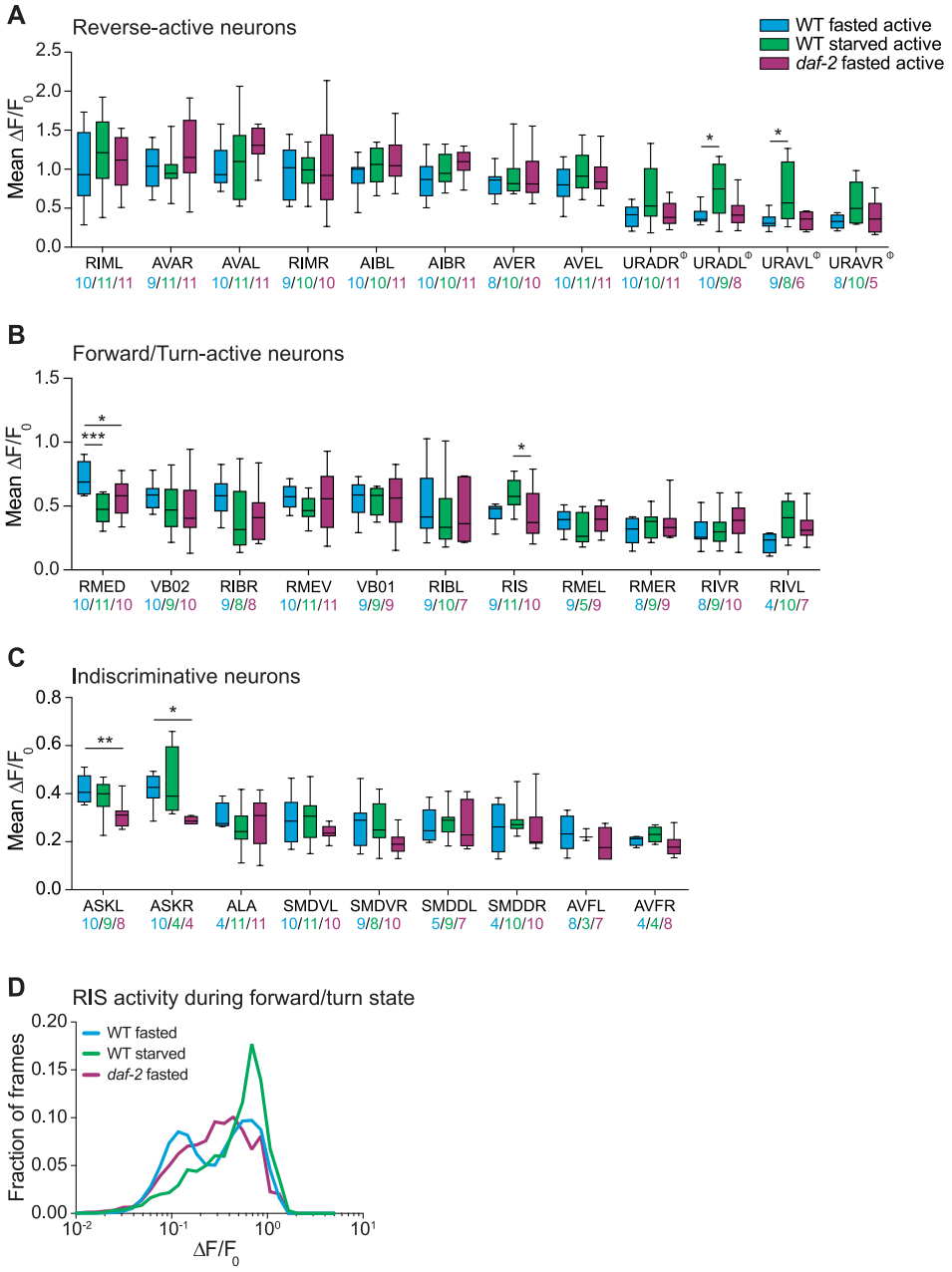

Figure S6. Starvation and mutation in *daf-2* affect the activities of a few neurons during active brain states. Related to Figures 4 and 6.

(A-C) Activity of neurons identified in ≥ 3 recordings. Activity for each neuron was measured during its principal motor command state: reverse-active neurons **(A)**, forward/turn-active neurons **(B)** or active indiscriminative of motor command state **(C)** in WT fasted, WT starved and *daf-2* fasted worms, respectively. Boxplots show median, interquartile range and min to max whiskers of mean $\Delta F/F_0$ during the principal active state. Labels indicate putative neuron IDs. Ambiguous IDs are denoted with Φ (see methods for alternatives). Number of data points for each neuron (n) indicated. For each neuron, all conditions were compared against each other using one-way ANOVA with Tukey's correction (*** p = 0.0002, ** p = 0.0046, * p ≤ 0.05). Significance levels are only indicated for significant comparisons.

(D) Fractional histograms (log scale) of all RIS $\Delta F/F_0$ values during the forward/turn brain state in WT fasted, WT starved and *daf-2* fasted animals. Number of experiments in which RIS could be identified: WT fasted n = 9, WT starved n = 11, *daf-2* fasted n = 10. Significant differences between the distributions were evaluated using a resampling test, see methods. The resulting p-values were corrected for multiple comparisons using the Bonferroni method and provide an estimate of the probabilities that the measured data in each condition have the same underlying distribution: $p = 3.9*10^{-5}$ (WT fasted versus WT starved), p = 0.0801 (WT fasted versus *daf-2* fasted), $p = 6.3*10^{-5}$ (WT starved versus *daf-2* fasted).

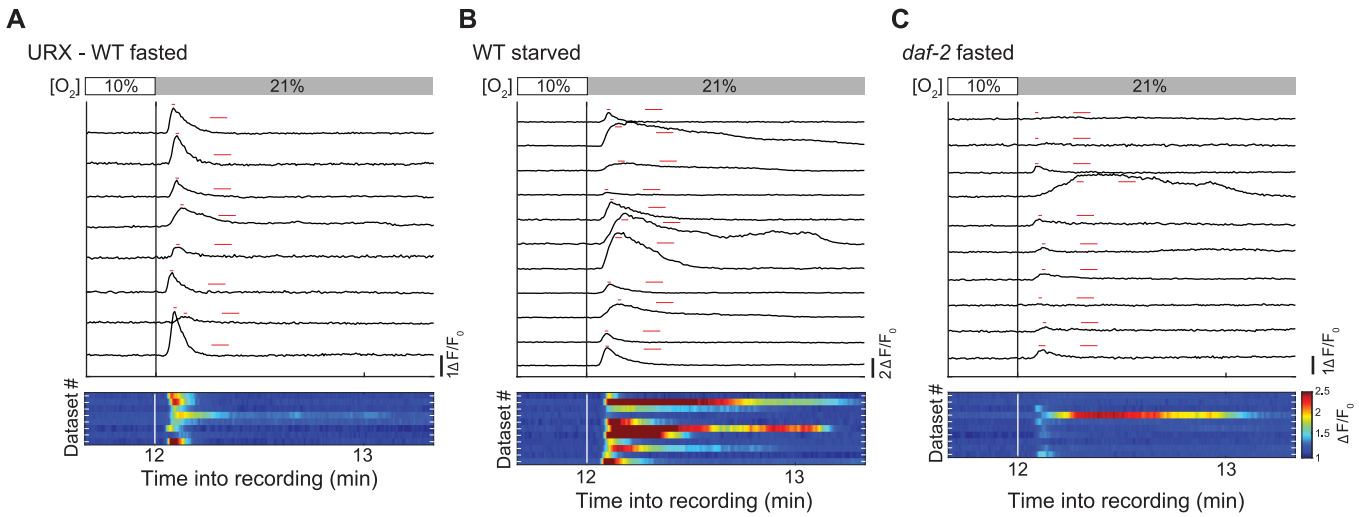

Figure S7. Starvation and *daf-2* modulate URX neuronal activity. Related to Figure 7.
Top: Activities of detected URX neurons per recording for WT fasted **(A)**, WT starved **(B)** and *daf-2* fasted **(C)** worms. Shown is the activity of a single URX neuron or, in case both neurons of the bilateral pair were detected, the mean of their activity. Red bars indicate intervals used for quantification in Figure 7D. Bottom: Heat map of URX neuronal activity corresponding to plots on top. O_2 stimulation as indicated.

Table S1. Candidate genetic screen in fasted animals reveals genes involved in O_2 downshift-induced quiescence. Related to Figure 2.

Quantified is fraction quiescent upon fasting during the time interval shown in Figures 1C and 2A for strains with number of experiments (n) ≥ 3. Genes are grouped in categories (indicated in bold) according to biological function and sorted alphabetically within each category.
Significance is determined using one-way ANOVA with Dunnett's correction. Strains significantly different from N2 are emphasized in red.

Gene (allele)	Mean fraction quiescent (± SEM)	Adjusted p-value
N2	0.0113 (± 0.003)	
Neuron differentiation		
ceh-10(ct78)	0.0004 (± 0.0004)	0.9996
ceh-23(ms23)	0.007 (± 0.0044)	0.9998
ceh-36(ks86)	0.0043 (± 0.0037)	0.9997
ceh-37(ok272)	0.003 (± 0.0019)	0.9997
che-1(p679)	0.0018 (± 0.0009)	0.9996
daf-10(e1387)	0.1604 (± 0.0133)	< 0.0001
lin-32(u282)	0.016 (± 0.008)	0.9998
mec-3(e1338)	0.0059 (± 0.0053)	0.9998
odr-3(n2150)	0.0159 (± 0.0103)	0.9998
odr-7(ky4)	0.0035 (± 0.0022)	0.9996
ttx-1(p767)	0.0483 (± 0.0268)	0.9979
ttx-3(mg158)	0.0011 (± 0.0006)	0.9996
unc-130(oy10)	0.00087 (± 0.00087)	0.9996
Growth factor signaling		
age-1(hx546)	0.0196 (± 0.019)	0.9996
akt-1(mg144)	0.0063 (± 0.0029)	0.9997
bra-1(nk1)	0.0043 (± 0.0024)	0.9997
daf-1(m40)	0.0388 (± 0.0187)	0.9986
daf-2(e1370)	0.3058 (± 0.0212)	< 0.0001
daf-3(e1376)	0 (± 0)	0.9996
daf-4(m63)	0.0246 (± 0.0156)	0.9994
daf-16(mu86)	0.0105 (± 0.0036)	0.9999
dbl-1(wk70)	0.0009 (± 0.0005)	0.9996
ins-1(nr2091)	0.0125 (± 0.0049)	0.9999
ins-7(tm1907)	0.0037 (± 0.0037)	0.9997
ins-10(tm3498)	0.0094 (± 0.0047)	0.9999
ist-1(ok2706)	0.0204 (± 0.0063)	0.9996
sma-6(e1482)	0.016 (± 0.0055)	0.9998
G protein signaling		
ags-3(ok1169)	0.1276 (± 0.0497)	0.0052
egl-30(ad806)	0.0021 (± 0.0021)	0.9996
egl-30(js126)	0.0078 (± 0.0055)	0.9999
gar-3(vu78)	0.0754 (± 0.0388)	0.5542
goa-1(sa734)	0.0221 (± 0.0082)	0.9996
gpa-6(pk480)	0.0088 (± 0.0044)	0.9999
gpa-8(pk345)	0.0246 (± 0.005)	0.9994
gpa-10(pk362)	0.0091 (± 0.0044)	0.9999
gpb-2(ad451)	0.0745 (± 0.0493)	0.5791
grk-2(gk268)	0.1204 (± 0.0276)	0.0123

grk-2(rt97)	0.2013 (± 0.0546)	< 0.0001
gsa-1(ce81)	0.0011 (± 0.0005)	0.9996
odr-4(n2144)	0.0075 (± 0.0075)	0.9999
rgs-2(vs17)	0.0077 (± 0.0025)	0.9998
Metabolism		
aak-2(gt33)	0.0017 (± 0.001)	0.9992
aak-2(rr48)	0.011 (± 0.0054)	0.9999
fat-3(wa22)	0.0092 (0.0024)	0.9999
nhr-49(ok2165)	0.0698 (± 0.0176)	0.7177
ogt-1(ok430)	0.0098 (± 0.0056)	0.9999
pept-1(lg1601)	0.0088 (± 0.0015)	0.9999
Neurotransmitter		
bas-1(tm351)	0.0058 (± 0.0017)	0.9997
cat-1(e1111)	0.0274 (± 0.0095)	0.9993
cat-2(e1112)	0.0321 (± 0.0203)	0.9996
cat-4(e1141)	0.0158 (± 0.0104)	0.9998
dat-1(ok157)	0.0046 (± 0.0014)	0.9997
dop-5(ok568)	0.0059 (± 0.0006)	0.9998
dop-6(ok2090)	0.0032 (± 0.0028)	0.9997
eat-2(ad465)	0.0076 (± 0.0034)	0.9999
eat-4(ky5)	0.0032 (± 0.0019)	0.9995
egl-3(n150)	0.0185 (± 0.0177)	0.9997
flp-34(ok3071)	0.005 (± 0.0003)	0.9997
glt-1(ok206)	0.0048 (± 0.0026)	0.9997
glt-3(bz34)	0.0113 (± 0.0055)	0.9999
glt-5(ok1987)	0.0113 (± 0.0054)	0.9999
glt-6(tm1316)	0.0201 (± 0.0096)	0.9996
glt-7(tm1641)	0.0156 (± 0.0046)	0.9998
nlp-15(ok1512)	0.0049 (± 0.0021)	0.9997
nmur-1(ok1387)	0.0028 (± 0.0018)	0.9997
nmur-2(ok3502)	0.0008 (± 0.0008)	0.9996
npr-9(tm1652)	0.0068 (± 0.0061)	0.9998
ntc-1(tm2385)	0.0173 (± 0.0086)	0.9997
ntr-1(tm2765)	0.0093 (± 0.0059)	0.9999
ntr-2(tm2243)	0.0158 (± 0.0088)	0.9998
sbt-1(ok901)	0.0047 (± 0.0028)	0.9997
ser-2(ok2103)	0.0086 (± 0.0029)	0.9999
tph-1(mg280)	0.0065 (± 0.0045)	0.9999
unc-31(e928)	0.0091 (± 0.0053)	0.9996
Various		
crh-1(tz2)	0.0133 (± 0.0046)	0.9999
daf-22(m130)	0.0049 (± 0.0042)	0.9997
egl-4(ad450)	0.0009 (± 0.0005)	0.9996
egl-4(n478)	0.0146 (± 0.0119)	0.9996
egl-9(sa307)	0.0559 (± 0.0227)	0.9789
inx-1(tm3524)	0.0105 (± 0.0068)	0.9999
inx-4(tm3276)	0.0024 (± 0.0024)	0.9996
inx-14(ag17)	0.0113 (± 0.0046)	0.9999
inx-19(ky634)	0.0659 (± 0.0058)	0.8239
itr-1(sa73)	0.0274 (± 0.0065)	0.9993
jkk-1(km2)	0.0784 (± 0.0375)	0.4727
ocr-2(ak47)	0.0026 (± 0.0001)	0.9996
trp-4(gk341)	0.0133 (± 0.0042)	0.9999

trp-4(ok1605)	0.0103 (± 0.0061)	0.9999
unc-43(n498n1186)	0.0062 (± 0.0052)	0.9998
unc-68(e540)	0.0096 (± 0.0049)	0.9999

Supplemental experimental procedures

Worm strains and maintenance

Worms were maintained under standard laboratory conditions on nematode growth medium (NGM) plates seeded with *Escherichia coli* OP50 as bacterial food source. Strains were kept at 20°C, except for strains carrying a temperature-sensitive conditional mutation (see below). The wild type strain used was *C. elegans* Bristol N2. All strains are listed in the table below.

Strain list. Strains are listed in order of appearance, followed by a list of strains exclusively used for candidate genetic screen (Table S1).

Strain	**Information**	**Genotype (and injection concentration, if applicable)**	**Source**
N2	wild type		Caenorhabditis Genetics Center
CX11697	genetic BAG and ASG ablation	*kyIs536[Pflp-17::p17::SL2::gfp; elt-2::mCherry]; kyIs538[Pglb-5::p12::SL2::gfp; elt-2::mCherry]*	Cori Bargmann, Rockefeller University
CX7102	genetic URX, AQR, PQR ablation	*lin-15(n765); qaIs2241[gcy-36::egl-1; gcy-35::gfp; lin-15(+)] X*	Cori Bargmann, Rockefeller University
CX11735	genetic BAG, ASG, URX, AQR, PQR ablation	*kyIs536[Pflp-17::p17::SL2::gfp; elt-2::mCherry]; kyIs538[Pglb-5::p12::SL2::gfp; elt-2::mCherry]; lin-15(n765); qaIs2241[gcy-36::egl-1; gcy-35::gfp; lin-15(+)] X*	Cori Bargmann, Rockefeller University
ZIM426	genetic RMG ablation	*mzmEx252[Pglr-4::p12::SL2::mCherry (25ng/µl); Punc-122::dsRed (15ng/µl)]; mzmEx251[Pncs-1::p17::SL2::mCherry (5ng/µl); Punc-122::gfp (15ng/µl)]*	This study
JY190		*osm-9(yz6) IV*	Caenorhabditis Genetics Center
CX6448		*gcy-35(ok769) I*	Cori Bargmann, Rockefeller University
AX2197		*gcy-36(db66) X*	Cori Bargmann, Rockefeller University
CB1370		*daf-2(e1370) III*	Caenorhabditis Genetics Center
CF1038		*daf-16(mu86) I*	Caenorhabditis Genetics Center
ZIM919		*daf-16(mu86) I; daf-2(e1370) III*	This study
JN1515	ubiquitous *daf-2* rescue	*daf-2(e1370) III; Ex[Pdpy-30::daf-2a; Pmyo-3::venus]*	Yuichi Iino, University of Tokyo, Ohno et al., 2014
ZIM1025	pan-neuronal *daf-2* rescue	*daf-2(e1370) III; mzmEx628[Prab-3::daf-2a::SL2::mCherry* (10ng/µl)*; Punc-122::dsRed* (15ng/µl)*]*	This study
ZIM1016	intestinal *daf-2* rescue	*daf-2(e1370) III; mzmEx620[Pges-1::daf-2a::SL2::mCherry* (30ng/µl)*; Punc-122::dsRed* (15ng/µl)*]*	This study
ZIM1341	inter-/motor neuron *daf-2* rescue	*daf-2(e1370) III; mzmEx813[Pglr-4::daf-2a::SL2::mCherry* (25ng/µl)*; Punc-122::dsRed* (15ng/µl)*]*	This study

ZIM1303	sensory neuron *daf-2* rescue	*daf-2(e1370) III; mzmEx790[Posm-9::daf-2a::SL2::mCherry::osm-9-3'UTR* (30ng/µl)*; Punc-122::dsRed* (15ng/µl)*]*	This study
ZIM1394	*Pflp-21 daf-2* rescue	*daf-2(e1370) III; mzmEx845[Pflp-21::daf-2a::SL2::mCherry* (20ng/µl)*; Punc-122::dsRed* (15ng/µl)*]*	This study
ZIM1580	*Pflp-21* reporter line	*daf-2(e1370) III; mzmEx943[Pflp-21::mCherry (20ng/µl); Punc-122::gfp (15ng/µl)]*	This study
ZIM1326	*Pflp-21* plus sensory neuron *daf-2* rescue	*daf-2(e1370) III; mzmEx801[Pflp-21::daf-2a::SL2::mCherry* (20ng/µl)*; Posm-9::daf-2a::SL2::mCherry::osm-9-3'UTR* (30ng/µl)*; Punc-122::dsRed* (15ng/µl)*]*	This study
ZIM1393	*Pglr-4; Posm-9* expression pattern overlap	*daf-2(e1370) III; mzmEx4[Pglr-4::gfp (30ng/µl); Punc-122::dsRed (15ng/µl)]; mzmEx790[Posm-9::daf-2a::SL2::mCherry::osm-9-3'UTR (30ng/µl); Punc-122::dsRed (15ng/µl)]*	This study
ZIM1206	ASI + URX, AQR, PQR *daf-2* rescue	*daf-2(e1370) III; mzmEx732[Pgpa-4::daf-2a::SL2::mCherry (40ng/µl); Pgcy-36::daf-2a::SL2::mCherry (1.5ng/µl); Punc-122::dsRed (15ng/µl)]*	This study
ZIM1048	WT whole-brain imaging line	*lite-1(ce314) X; mzmIs4[Punc-31::NLS-GCaMP5K; Punc-122::gfp]*	Kato et al., 2015
ZIM1107	*daf-2* whole-brain imaging line	*daf-2(e1370) III; lite-1(ce314) X; mzmIs4[Punc-31::NLS-GCaMP5K; Punc-122::gfp]*	This study
ZIM1181	ASK marker whole-brain imaging line	*lite-1(ce314) X; mzmIs4[Punc-31::NLS-GCaMP5K; Punc-122::gfp]; mzmEx706[Psrbc-64::NLSwCherryNLS* (25ng/µl)*; Punc-122::dsRed* (15ng/µl)*]*	This study
Strains exclusively used for candidate genetic screen (Table S1)			
Strain	**Genotype**	**Additional information**	**Source**
ZIM177	*aak-2(gt33) X*	6x outcrossed from strain TG33 (Caenorhabditis Genetics Center)	This study
MR507	*aak-2(rr48) X*		Caenorhabditis Genetics Center
TJ1052	*age-1(hx546) I*		Caenorhabditis Genetics Center
RB1145	*ags-3(ok1169) X*		Caenorhabditis Genetics Center
GR1310	*akt-1(mg144) V*		Caenorhabditis Genetics Center
LC33	*bas-1(tm351) III*		Caenorhabditis Genetics Center
NU1	*bra-1(nk1) X*		Caenorhabditis Genetics Center
CB1111	*cat-1(e1111) X*		Caenorhabditis Genetics Center
CB1112	*cat-2(e1112) II*		Caenorhabditis Genetics Center
CB1141	*cat-4(e1141) V*		Caenorhabditis Genetics Center
BW506	*ceh-10(ct78) III*		Caenorhabditis Genetics Center
OH149	*ceh-23(ms23) III*		Caenorhabditis Genetics Center

FK311	*ceh-36(ks86) X*		Caenorhabditis Genetics Center
LJ1	*ceh-37(ok272) X*		Caenorhabditis Genetics Center
PR679	*che-1(p679) I*		Caenorhabditis Genetics Center
YT17	*crh-1(tz2) III*		Caenorhabditis Genetics Center
DR40	*daf-1(m40) IV*		Caenorhabditis Genetics Center
CB1376	*daf-3(e1376) X*		Caenorhabditis Genetics Center
DR63	*daf-4(m63) III*		Caenorhabditis Genetics Center
CB1387	*daf-10(e1387) IV*		Caenorhabditis Genetics Center
DR476	*daf-22(m130) II*		Caenorhabditis Genetics Center
RM2702	*dat-1(ok157) III*		Caenorhabditis Genetics Center
LT121	*dbl-1(wk70) V*		Caenorhabditis Genetics Center
RB785	*dop-5(ok568) V*		Caenorhabditis Genetics Center
RB1680	*dop-6(ok2090) X*		Caenorhabditis Genetics Center
DA465	*eat-2(ad465) II*		Caenorhabditis Genetics Center
CX13503	*eat-4(ky5) III*		Cori Bargmann, Rockefeller University
CX9191	*egl-3(n150) V*		Cori Bargmann, Rockefeller University
DA521	*egl-4(ad450) IV*		Caenorhabditis Genetics Center
MT1073	*egl-4(n478) IV*		Caenorhabditis Genetics Center
JT307	*egl-9(sa307) V*		Caenorhabditis Genetics Center
DA1084	*egl-30(ad806) I*		Caenorhabditis Genetics Center
NM1380	*egl-30(js126) I*		Caenorhabditis Genetics Center
BX30	*fat-3(wa22) IV*		Caenorhabditis Genetics Center
RB2269	*flp-34(ok3071) V*		Caenorhabditis Genetics Center
JD217	*gar-3(vu78) V*		Caenorhabditis Genetics Center
ZIM637	*glt-1(ok206) X*	isolated from strain ZB1106 (Caenorhabditis Genetics Center)	This study
ZIM648	*glt-3(bz34) IV*		Itzhak Mano, City University of New

			York, Mano et al., 2007
RB1615	*glt-5(ok1987) II*		Caenorhabditis Genetics Center
ZIM728	*glt-6(tm1316) IV*	5x outcrossed from strain FX01316 (National Bioresource Project)	This study
ZIM711	*glt-7(tm1641) IV*	4x outcrossed from strain FX01641 (National Bioresource Project)	This study
DG1856	*goa-1(sa734) I*		Caenorhabditis Genetics Center
NL1146	*gpa-6(pk480) X*		Caenorhabditis Genetics Center
NL1142	*gpa-8(pk345) V*		Caenorhabditis Genetics Center
NL1147	*gpa-10(pk362) V*		Caenorhabditis Genetics Center
DA541	*gpb-2(ad541) I*		Caenorhabditis Genetics Center
FG7	*grk-2(gk268) III*		Caenorhabditis Genetics Center
HA865	*grk-2(rt97) III*		Caenorhabditis Genetics Center
KG421	*gsa-1(ce81) I*		Caenorhabditis Genetics Center
CX7155	*ins-1(nr2091) IV*		Cori Bargmann, Rockefeller University
FX01907	*ins-7(tm1907) IV*		National Bioresource Project
FX03498	*ins-10(tm3498) V*		National Bioresource Project
CX12016	*inx-1(tm3524) X*		Cori Bargmann, Rockefeller University
FX03276	*inx-4(tm3276) V*		National Bioresource Project
AU98	*inx-14(ag17) I*		Caenorhabditis Genetics Center
CX6161	*inx-19(ky634) I*		Caenorhabditis Genetics Center
RB2621	*ist-1(ok2706) X*		Caenorhabditis Genetics Center
JT73	*itr-1(sa73) IV*		Caenorhabditis Genetics Center
KU2	*jkk-1(km2) X*		Caenorhabditis Genetics Center
TU282	*lin-32(u282) X*		Caenorhabditis Genetics Center
CB1338	*mec-3(e1338) IV*		Caenorhabditis Genetics Center
RB1716	*nhr-49(ok2165) I*		Caenorhabditis Genetics Center
VC1063	*nlp-15(ok1512) I*		Caenorhabditis Genetics Center

RB1288	*nmur-1(ok1387) X*		Caenorhabditis Genetics Center
RB2526	*nmur-2(ok3502) II*		Caenorhabditis Genetics Center
IC683	*npr-9(tm1652) X*		Caenorhabditis Genetics Center
FX02385	*ntc-1(tm2385) X*		National Bioresource Project
FX02765	*ntr-1(tm2765) I*		National Bioresource Project
FX02243	*ntr-2(tm2243) I*		National Bioresource Project
CX4544	*ocr-2(ak47) IV*		Caenorhabditis Genetics Center
CX2205	*odr-3(n2150) V*		Caenorhabditis Genetics Center
MT5300	*odr-4(n2144) III*		Caenorhabditis Genetics Center
CX4	*odr-7(ky4) X*		Caenorhabditis Genetics Center
RB653	*ogt-1(ok430) III*		Caenorhabditis Genetics Center
BR2742	*pept-1(lg1601) X*		Caenorhabditis Genetics Center
LX160	*rgs-2(vs17) X*		Caenorhabditis Genetics Center
RB987	*sbt-1(ok901) V*		Caenorhabditis Genetics Center
RB1690	*ser-2(ok2103) X*		Caenorhabditis Genetics Center
CB1482	*sma-6(e1482) II*		Caenorhabditis Genetics Center
MT15434	*tph-1(mg280) II*		Caenorhabditis Genetics Center
VC818	*trp-4(gk341) I*		Caenorhabditis Genetics Center
VC1141	*trp-4(ok1605) I*		Caenorhabditis Genetics Center
PR767	*ttx-1(p767) V*		Caenorhabditis Genetics Center
OH8	*ttx-3(mg158) X*		Caenorhabditis Genetics Center
DA509	*unc-31(e928) IV*		Caenorhabditis Genetics Center
MT2605	*unc-43 (n498n1186) IV*		Caenorhabditis Genetics Center
CB540	*unc-68(e540) V*		Caenorhabditis Genetics Center
PY1133	*unc-130(oy10) II*		Caenorhabditis Genetics Center

Note on genetic RMG ablation strain (ZIM426):
The two promoters used for split caspase expression (Chelur and Chalfie, 2007) in RMG also overlapped in additional neurons posterior to the nerve ring, likely SMDV or SAAV; occasional overlap in an additional neuron class was observed, likely AVH or AVJ. Therefore, these neurons might be ablated as well.

Molecular biology and transgenesis
Promoters were PCR-amplified from either whole-worm genomic DNA or indicated plasmid (see table below) and, flanked by restriction sites, cloned into pSM vector. Promoters were inserted using *FseI* and *AscI* restriction sites. For the *Posm-9* construct, the *unc-54* 3'UTR of pSM vector was replaced with *osm-9* 3'UTR.
A plasmid containing *daf-2a* cDNA was kindly provided by the Iino laboratory (Ohno et al., 2014). *daf-2a* cDNA was amplified from this plasmid and inserted into pSM vector using *NheI* and *KpnI* restriction sites.
Transgenic lines were generated using standard microinjection techniques. In brief, plasmids were injected into the gonads of young adult hermaphrodites, thereby generating heritable extrachromosomal arrays. All injection mixes contained a total of 100 ng/µl DNA. All plasmids are listed in the table below.

Oligonucleotides used for amplification of tissue- and cell-specific promoter fragments. Fwd indicates forward primer, Rev indicates reverse primer sequence. Number in brackets shows the length of the generated fragment.

Gene	Sequence (5' → 3')	Notes
ges-1	Fwd: GCATAGCCCGCAGTCAC Rev: CTGAATTCAAAGATAAGATATGTAATA (1931 bp)	amplified from plasmid pJH668, a kind gift from the Zhen lab
rab-3	Fwd: GATCTTCAGATGGGAGCA Rev: CTGAAAATAGGGCTACTG (1208 bp)	
glr-4	Fwd: GGAGCACAAACGAGAAGACC Rev: GCTGTGTAAAAGTTTAGCTCATC (4392 bp)	
osm-9	Promoter Fwd: ACGTACGATTATCTGTTGCG Promoter Rev: CCAATTTTTTCAGAAACCAAAC (1744 bp) 3'UTR Fwd: GAACTTTTTTCTTCTA 3'UTR Rev: TCGTCTCTATTTCTAAATTGC (3520 bp)	
flp-21	Fwd: TGAGGTCACGCAACTTGATGATC Rev: GAAAATGACTTTTTGGATTTTGG (4099 bp)	amplified from plasmid pEM1, a kind gift from the Bargmann lab
gcy-36	Fwd: ATGATGTTGGTAGATGGGGTTTGG Rev: AAATTCAAACAAGGGCTACCCAACA (1087 bp)	
gpa-4	Fwd: CGATGATCATTGGAAATGCGGTTTCC Rev: TGTTGAAAAGTGTTCACAAAATGAATAAGTGG (2783 bp)	

Expression patterns of promoters used for transgenic rescues
Pdpy-30: ubiquitous (Ohno et al., 2014)
Pges-1: intestine (Hung et al., 2014)
Prab-3: pan nervous system (Nonet et al., 1997)
Pglr-4: AVA, RMD, SMD, SAA, SIB, RIB, RIM, AVH, FLP, RMG, DVA, AUA, PVD, URY, URA, SAB, RIF, DB, PVU (Brockie et al., 2001)
Posm-9: OLQ, IL2, AWA, AWC, ASE, ADF, ASG, ASH, ASI, ASJ, ASK, ADL, FLP, PVD, PHA, PHB (Colbert et al., 1997)
Pflp-21: RMG (100%), ASJ (100%), URA (100%), FLP (100%), M2 (100%), URX (80%), ASI (10%), 2-3 tail neurons (100%) (assessed using a *daf-2(e1370); Pflp-21::mCherry* reporter line)
Pgpa-4: ASI (Jansen et al., 1999)
Pgcy-36: URX, AQR, PQR (Gray et al., 2004)

Plasmid list.

Plasmids used in this study (plasmid no)	Source
Pglr-4::p12::SL2::mCherry (pRL87)	This study
Pncs-1::p17::SL2::mCherry (pRL58)	This study
Prab-3::daf-2a::SL2::mCherry (pSS92)	This study
Pges-1::daf-2a::SL2::mCherry (pSS91)	This study
Pglr-4::daf-2a::SL2::mCherry (pSS96)	This study
Posm-9::daf-2a::SL2::mCherry::osm-9 3'UTR (pFM5)	This study
Pflp-21::daf-2a::SL2::mCherry (pFM6)	This study
Pglr-4::gfp (pIH4)	This study
Pgpa-4::daf-2a::SL2::mCherry (pFM4)	This study
Pgcy-36::daf-2a::SL2::mCherry (pFM2)	This study
Psrbc-64::NLSwCherryNLS (pTS113)	Kato et al., 2015
Pflp-21::mCherry (pRL49)	This study
Punc-122::dsRed	Cori Bargmann, Rockefeller University
Punc-122::gfp	Cori Bargmann, Rockefeller University

Worm population behavioral recordings

Worm population behavioral recordings were performed at 20°C as described previously (Hums et al., 2016; Zimmer et al., 2009), with some modifications. For each assay, ~100 one-day old adult hermaphrodites were manually transferred onto a bacteria-free 14 cm NGM agar assay plate. For well-fed assays, transfer time was kept consistent and limited to 10 minutes. Well-fed assays were started 12-14 minutes after the start of assay preparation. For fasted assays, the same animals and plates as for well-fed assays were re-examined. For starved assays, animals were transferred to 15 cm glass petri dishes containing NGM agar plus 25 µg/ml carbenicillin to prevent growth of bacterial food sources during starvation period. Animals were transferred from starvation plates to NGM assay plates after 15 hours of starvation and allowed to settle for one additional hour before the assay commenced. Animals were constrained to a recording region (56 x 56 mm) by creating an arena that was delimited by Whatman filter paper soaked in 20 mM of the repellent copper chloride. Gas flow was achieved by placing a custom-made plexiglass device with a flow arena of 60 x 60 x 0.7 mm onto the assay arena. Gas flow was set to 100 ml/min and controlled using a static gas mixer connected to mass flow controllers (Vögtlin Instruments AG) that were operated by custom-written LabVIEW software (National Instruments). The recording area was illuminated with a 200 mm x 200 mm flat red LED. Recordings were acquired at 3 frames per seconds (fps) on a 4-5 megapixel CCD camera (JAI) using StreamPix software (NorPix). Pixel resolution was 0.0276 mm/pixel.

Temperature-sensitive *daf-2(e1370)* mutants, all *daf-2* rescue strains and corresponding N2 controls were maintained at the permissive temperature of 16°C to prevent developmental arrest (Gems et al., 1998). For well-fed and fasted assays, food plates with animals were shifted to 25°C in the evening before the experiment, allowing a minimal time of 16 hours at the restrictive temperature. The food plates were placed in the experiment room (20 ± 1°C) 2 hours before the start of the experiment to avoid artefacts due to sudden temperature shifts. The subsequent preparation of well-fed and fasted assays was performed as described above for non-temperature-sensitive strains. For starved experiments, food plates with animals were shifted to restrictive 25°C approximately 7 hours before starvation commenced. Animals were then transferred onto pre-warmed starvation plates and starved at 25°C. After 14 hours of starvation, starved plates were placed in the experiment room to accommodate animals to the ambient temperature in the room. After 15 hours, starved animals were transferred onto the assay plate and allowed to settle for one additional hour, as described above for non-temperature-sensitive strains. The gas flow rate for temperature-sensitive strains and their controls was adjusted to 50 ml/min to minimize their arena-leaving behavior.

For experiments shown in Figures 1E and 1F, worms were transferred from the starvation plates to the assay plates after 14 hours of starvation, allowed to settle for one additional hour as described above and the recordings were started after 15 hours of starvation.

All gas mixtures were balanced with nitrogen (N_2).

For the data shown in Figure S1B and Movie S1, worm population recordings were performed using the same setup, with some modifications to obtain higher spatial and temporal resolution (pixel resolution: 0.0129 mm/pixel, frame rate: 10 frames per second), as described previously (Hums et al., 2016). The recording region for these experiments

was 36 x 36 mm and gas flow with a flow rate of 25 ml/min was achieved using a plexiglass device with a flow arena of 39 x 39 x 0.7 mm. Single movie frames shown in Figures 1A-1D were taken from experiments performed with these settings.

Video tracking of animal behavior

Tracking and analysis were performed using customized MATLAB scripts that are based on the Parallel Worm Tracker (Hums et al., 2016; Ramot et al., 2008; Zimmer et al., 2009). In brief, each frame was converted into a binary image using an intensity threshold. Worms were identified as objects in a defined size range. The worm's centroid was determined using the MATLAB regionprops function and worm trajectories over time were created by connecting nearby centroid coordinates in adjacent frames. For each identified worm object, centroid coordinates as outlined above, size in pixels, direction in degrees, speed and eccentricity were calculated. Trajectories were terminated when objects collide with each other or with the boundaries of the arena. Trajectories below a length of 20 frames (i.e. 6.67 sec) were discarded. The behavior of each worm is therefore represented by several worm tracks of varying lengths but not overlapping in time.

Worm speed was calculated by smoothing the worm trajectories. The worm speed in each track was normalized to the median size of N2 wild type worms to account for speed variability arising from difference in size. Backward locomotion (= reversals) was detected by characteristic changes in angular velocity. Omega turns (= deep body bends leading to re-orientation) were detected based on the co-occurrence of an increase in angular velocity and a decrease in eccentricity within a specific range. Reversal and omega turn frequencies were calculated in bins of 45 frames (= 15 seconds). Average speed and average reversal frequencies shown are calculated only from worms that were in their active phase (except for Figure S2D), i.e. data points at which a worm was found to be quiescent or head-waving were taken out from the calculation. Speed data only contain forward movement, i.e. in addition to excluding quiescent/head-waving periods, time points at which worms were found reversing or turning were excluded from calculations.

Determination of quiescence and head-waving episodes

We distinguished 2 immobile states: quiescence (Q) and head-waving (H), the latter of which was characterized by retained dorso-ventral movement of the head/neck region. Both states were determined in 1 sec bins. Tracks of less than 60 frames (i.e. 20 sec) as well as tracks in which the mean speed over the entire track was less than 0.006 mm/s were excluded to avoid tracking of dead objects. The state detection relied on threshold values of speed (1 sec binning) and the instantaneous change in object eccentricity ($d\varepsilon/dt$) (1 sec binning and subsequently smoothed using a 5 sec running average) to detect head and body movement. Thresholds were as follows and determined empirically: 0.02 (Q) and 0.025 (H) for speed and 0.00107 (Q and H) for $d\varepsilon/dt$ (Figure S1C). Quiescence was determined for the center frame of a 10 sec sliding window if animals exceeded the Q thresholds for less than 20% of time in the sliding window. Head-waving was determined by animals exceeding the H speed and $d\varepsilon/dt$ thresholds for $< 20\%$ and $> 80\%$ of time in a 20 sec sliding window, respectively. Quiescence (head-waving) episodes required to be at least 10 (15) sec in length. The minimal length thresholds for quiescence and head-waving have been determined empirically by manual inspection of behavioral recordings of individual worms. During these inspections, we found that there existed lasting and continuous episodes that were characterized by low speed in combination with either the presence or absence of head movement. The thresholds allow to find these states as 'pure' states as opposed to e.g. quiescence periods that are frequently interspersed with short head movements.

It should be noted that the resolution of the experimental setup did not allow unambiguous distinction of quiescence and head-waving states, because eccentricity changes due to head-waving could only be detected if the head moved in x-y direction. Movement in z is unreliably resolved and some head-waving periods might falsely be assigned to quiescence.

All plots and quantifications showing activity and quiescence, respectively, exclude head-waving behavior.

Skeletonization and segment angle time series

This analysis was performed on behavioral data recorded at higher temporal and spatial resolution (see 'Worm population behavioral recordings'). To obtain the segment angle time series depicted in Figure S1B, the binary worm images resulting from the image processing during tracking (see 'Video tracking of animal behavior') were skeletonized as described previously (Hums et al., 2016), resulting in 25 equally spaced body segments. The angles shown in Figure S1B represent intersegment angles between adjacent body segments from head (segment angle 1) to tail (segment angle 24). Small gaps (up to 4 frames) in the depicted angles time series were interpolated using cubic interpolation. Angles were smoothed over 6 frames (i.e. 0.6 sec) for visualization.

Data presentation
For graphs displaying trial-averaged behavior data, the mean represents the mean across all tracks across all assays (typically ~100 animals per assay). For speed and reversal data, the standard error accounts for track-to-track variability. For graphs displaying fraction quiescent or head-waving, the mean represents the mean fraction across experiments and the standard error accounts for experiment-to-experiment variability. For visualization, speed and quiescence data are shown in 15 frames (= 5 seconds) bins and reversals are shown in 45 frames (= 15 seconds) bins. All intervals for behavior quantification were chosen to optimally reflect the behavior in question. For reversals, the interval of maximal change upon O_2 downshift is quantified; these time points were slightly different for each feeding state but consistent across genotypes. To display speed recovery, three time points needed to be quantified and set in relation to each other: basal speed ($Speed_{max}$, indicated by black bar in Figures 1B and S3A), minimum speed immediately following O_2 downshift ($Speed_{min}$, red bar in Figures 1B and S3A) and sustained speed towards the end of O_2 downshift ($Speed_{sust}$, cyan bar in Figures 1B and S3A). For calculation of speed recovery, the absolute sustained speed ($Speed_{sust}$) was normalized to a linear scale using the formula: $(Speed_{sust} - Speed_{min})/(Speed_{max} - Speed_{min})$. For the quantification of quiescence and head-waving behavior, we quantify steady state levels, i.e. once they have established upon O_2 downshift.

All statistical analyses of behavioral data (Figures 1, 2, S1A, S1D, S1E, S1G, S2D, S3A and S3C-S3E) were performed to account for experiment-to-experiment variability, i.e. each data point used for generating bar graphs or box plots was a population average calculated from each individual experiment. Statistical tests were applied as described below under 'Quantification and Statistical Analysis'.

State transition diagrams
For each active (A), head-waving (H) and quiescent (Q) state outbound rates of state transitions were calculated as per second probabilities. Behavioral states were determined in bins of 1 sec. For each track, the sum of events of every possible transition was calculated. From all active, head-waving and quiescent states 4 transition paths were possible (i.e. into the remaining two states, self-transition, and transition into an undefined state). Undefined states corresponded to time points at which active states were interrupted but the lengths of the detected bouts did not reach threshold values to be designated neither quiescent nor head-waving. Transition rates were calculated per experiment by summing all transition events of one kind (e.g. AA) and dividing by the total number of transition events from the same state of origin (e.g. AA + AH + AQ). Transitions into NaN were neglected.

Feeding quiescence
Individual starved worms were examined under a stereomicroscope for 60 sec. Quiescence during the observation period needed to last for at least 10 sec to be considered a quiescent episode. Worms during quiescent episodes (n = 20 worms, 28 quiescent episodes) were scored for pumping, as judged by movement of the terminal pharyngeal bulb. Worms that were quiescent for the entire 60 sec observation period were touched with a worm pick to confirm reversibility of quiescence. Scored worms were removed from the plate to avoid second examination. A total number of 3 pumps was counted across all worms and quiescent episodes. All pumps occurred during quiescence episodes that spanned the entire 60 sec observation period. 1 worm exhibited 2 pumps that occurred spaced by approximately 20 sec; the third pump occurred as a single event in a different worm.

Approximating worm posture by eccentricity
We used absolute eccentricity values in 1 sec bins for time points at which tracks were identified as either quiescent or active. Of the active time points, we only considered fast movement (speed > 0.1 mm/sec) and excluded time points at which the animal was found to engage in pirouette behavior (i.e. performing reversals or turns). This allowed to compare quiescent animals to their posture-wise most similar counterpart (i.e. worms that move rapidly forward by propagation of sinusoidal waves). Eccentricity was chosen to be displayed as $1-\varepsilon$ to aid subsequent visualization. Eccentricity values were binned in increments of 0.005 and the cumulative sum of the binned data was calculated. Significance was determined by a customized resampling test in MATLAB. For each of the 28 experiments, eccentricity values for all bins were pooled and equal numbers of samples as originally observed were randomly drawn without replacements to obtain two test cumulative density functions (CDF), like for the original data shown in Figure S1C. Then we calculated the L_1 distance (i.e. absolute difference) between the 2 test CDFs. This resampling procedure was performed 10^6 times for each experiment (n = 28) and p_n, which is the fraction of distances equal to or larger than the original one, was recorded for each of the n = 28 runs. The final p-value is the mean of $p_{n(1-28)}$.

Reversal probabilities of active and quiescent worms
For this analysis, the quiescent state was detected in 10 sec bins rather than sliding windows in order to obtain temporally precise boundaries. Worms that were either active or quiescent for 2 min prior to O_2 upshift and for which the track continued for at least 1 min following O_2 upshift were used. Reversals were calculated in 2 sec bins for each track and are shown as mean fraction of animals reversing across experiments.

Determination of behavioral state bouts and correlations
Bouts were extracted from tracks with a minimal track length of 1800 sec (median track length: 4682 sec) during the 10% O_2 period (earliest starting at minute 45) of the experiments shown in Figure 1F. The median length of behavioral state bouts was 40-70 sec but the distribution of all detected states (active, head-waving, quiescent) exhibited long-tailed distributions with bout lengths of up to 30 min, leading to a non-Gaussian distribution of the data. Only subsets of all detected bouts were used for correlation analyses (Figures S2E-S2H): we excluded bout pairs in which either the preceding bout started with the beginning of the track or the succeeding bout was interrupted by the track end, respectively, in order to ensure that our analysis only included complete bouts. Since quiescence periods were often directly preceded or followed by head-waving bouts, we allowed for a head-waving period of average length (60 sec) to separate active from succeeding quiescence bouts (and vice versa).
Axes cropping of scatter plots omitted data points, which were included in correlation analysis. Number of data points cropped: 3 (Figure S2E, S2F), 32 (Figure S2G), 6 (Figure S2H). Due to the non-normality of the underlying data, correlations and p-values were calculated using the Spearman rank correlation test in GraphPad Prism.

Pharyngeal pumping
WT and *daf-2(e1370)* mutant worms were shifted to 25°C in the evening before the experiment. Also in the evening before the experiment, thin NGM agarose pads (created by pouring melted agarose into a ring 2.45 mm thick and 50 mm in diameter and enclosed with glass on both sides to allow hardening into a smooth surface, as described previously (Kato et al., 2015)) were seeded with 50 µl of an *E. coli* OP50 overnight culture and kept at 37°C overnight. In the morning, the agarose pads were brought to the experiment room and allowed approximately 30 min to acclimate to the room temperature. Worms were kept at 25°C until used. Worms were placed on the agarose pad and allowed to adapt to the pad and room conditions for 15-25 min before the recording started. Prior to the recording, the agarose pad was placed inside an imaging chamber previously described for Ca^{2+} imaging in freely-moving worms (Kato et al., 2015) and covered with a 0.55 mm thick glass slide 0.7 mm from the agarose surface. The chamber containing the agarose pad was then placed onto a motorized stage with associated controller (MS-2000-PhotoTrack, Applied Scientific Instrumentation), allowing to follow the worm as it moved freely on the food lawn. Brightfield images were acquired for 4-4.5 min at an inverted compound microscope (Zeiss Axio Observer Z1) using an EMCCD camera (Evolve 512, Photometrics) and a 10x objective (Zeiss Plan-APOCHROMAT, NA 0.45) at 30 Hz using VisiView software (Visitron Systems GmbH, Germany). For each worm, pumping was counted as contractions of the terminal pharyngeal bulb for two 30 sec periods and each data point represents the average of both periods.

Determining overlap in expression pattern
The overlap in expression pattern between the *Pglr-4* and *Posm-9* promoter fragments was determined by taking z-stacks in a strain that was generated by crossing the *Posm-9::daf-2a::SL2::mCherry* rescue strain to a *Pglr-4::gfp* reporter line. Images were taken at an inverted spinning disk microscope (UltraViewVoX, PerkinElmer), equipped with an EMCCD camera (C9100-13, Hamamatsu). The overlap was determined by analyzing each z-plane individually using Fiji software and no coexpression of gfp and mCherry could be detected. *Posm-9* and *Pglr-4* are reported to overlap in their expression in FLP (Brockie et al., 2001; Colbert et al., 1997); however, we were unable to detect any overlap, suggesting lack of FLP expression under one of the promoters or expression below the detection limit.

Imaging of brain-wide neural activity in microfluidic chip
Imaging of brain-wide neural activity was done as described previously (Kato et al., 2015). Two-layer PDMS microfluidic devices were used to immobilize and stimulate worms (Schrödel et al., 2013; Zimmer et al., 2009). The worm channel was connected to a syringe containing 1 mM Tetramisole in NGM buffer. The microfluidic device was connected to the syringe using Tygon or polyethylene tubing. Worms were food-deprived on NGM agar plates as described for the worm population behavioral recordings. Illumination and piezo stage were started 2 min prior to image acquisition. Images were acquired at an inverted spinning disk microscope (UltraView VoX, PerkinElmer), equipped with an EMCCD camera (C9100-13, Hamamatsu). Images were acquired at 2 µm spacing over 12-15 z-planes, depending on the feeding state and, hence, size of the animal. These settings translated into an acquisition rate

of 1.6-2.6 volumes per second. Gas flow at a rate of 50 ml/min was achieved and controlled as described for the worm population behavioral recordings. The stimulus protocol used was identical to the behavioral paradigm (6min 21% O_2 – 6min 10% O_2 – 6min 21% O_2). All gas mixtures were balanced with N_2.
For each condition (WT fasted, WT starved, *daf-2* fasted), 6 datasets were generated from which neural traces of all detected neurons were extracted. These datasets were used for analyses on brain-wide changes and to perform principal component analysis (Figures 3A-3C, 4A, 5, 6A, 6B, 6D and S4). Furthermore, neural traces of spontaneously active sensory neurons (Figures 4B and 6E) were exclusively extracted from those datasets. To increase statistical power for some analyses, additional datasets were generated (in total: WT fasted = 10, WT starved = 11, *daf-2* fasted = 11) from which only neural traces of identifiable neurons were extracted, which include all neurons used to classify quiescent versus active brain states; these data in combination with the complete datasets were used for Figures 3D, 3E, 4C, 6C, 6F, 7, S5, S6 and S7. For datasets of WT starved at constant 21% O_2, only traces of neuronal classes required to determine the brain state were extracted (Figure 3E).

Neural time series extraction
Tracking and analysis of brain-wide imaging recordings was done as described previously (Kato et al., 2015), using custom MATLAB scripts. Briefly, ROIs were detected as local maxima in a noise- and motion-corrected reference ROI movie using a thresholding approach. The reference movie was generated by averaging successive blocks of movie frames. The number of averaged frames was chosen depending on the degree of movement in the recording and ranged from 40-100. ROIs in adjacent reference movie frames were joined based on closest distance relative to global inter-frame motion, thereby creating time-varying ROIs. ROIs present in adjacent z-planes were joined to create one spacetime voxel set. The adjoining process of all detected ROIs was proof-checked manually, falsely joined or created ROIs removed if necessary, and neurons that remained undetected during the automatic process were added manually.
Neuronal traces were extracted as z-plane-specific background-subtracted fluorescence intensity maxima at every time point. $\Delta F/F_0$ as calculated here uses the mean fluorescence intensity across a trial for each neuron as F_0. For BAG and URX O_2-sensory neurons (Figures 7A-7D and S7), which have lowest calcium at 21% and 10% O_2, respectively, $\Delta F/F_0$ was recalculated using the lowest 20% of fluorescence intensity values during a 60 sec period at 21% (BAG: 730-790 sec into recording) and 10% O_2 (URX: 370-430 sec into recording), respectively. All neural traces used here were de-trended to account for fluorophore bleaching.

Identification of head ganglia neurons
Between 114 and 149 neurons were detected in the head ganglia region of each WT recording, corresponding to 58%-76% of expected neurons. The number of detected neurons was slightly lower in *daf-2* animals (103-117 neurons, i.e. 53%-60%) due to the longer body size of *daf-2* mutants and thus fewer neurons in the field of view. Identification of neurons was based on their position relative to other neurons as well as their activity pattern (Kato et al., 2015). We confirmed the identity of ASK using the *Psrbc-64* marker (Kim et al., 2009). Some neuron identities remained ambiguous; these neuron classes are denoted with 'ϕ' and alternative identities are listed in brackets here: URA (URY, IL1), URY (URA, IL1).

Trace state annotation by segmentation
Neural time series were segmented into rise – high – fall – low phases as described previously (Kato et al., 2015). In brief, rise and fall phases of neurons were assigned when the time derivatives of $\Delta F/F_0$ traces were above and below a threshold of 5% of a neuron's full dynamic range, respectively. High and low phases were assigned to the in-between periods when $\Delta F/F_0$ remained at high or low values respectively, leading to the phase order rise – high – fall – low or rise – fall – low for some neurons (e.g. SMD or RIV). The global motor command state (forward – reverse – turn (dorsal or ventral)) corresponds to the low – rise + high – fall phases of AVA.

Brain state determination
Active and quiescent brain states were determined as described previously (Nichols et al., 2017). Briefly, quiescent brain states were defined by the absence of activity across 4 neuronal classes that unambiguously define motor behavior in freely behaving animals (Kato et al., 2015): fall and low phases in AVA, VB01 or VB02, SMDV, RIV and SMDD. Quiescence periods in Figures 3D, 3E and 6C were quantified as fraction of time spent in the quiescent brain state in 1 min bins.

Principal component analysis

Principal component analysis (PCA) was performed as described previously (Kato et al., 2015), with some modifications. Total-variation regularization (Chartrand, 2011) was used to compute de-noised time derivatives of $\Delta F/F_0$ neural traces. Each trace was normalized by the peak magnitude of their non-derivative $\Delta F/F_0$ time series. O_2-sensory, AVF and ASK neurons were excluded from the analysis, as were neurons that showed sudden strong, uncorrelated and nonrecurring activity. For generating phase plots, all neuronal time series data were projected onto the first 3 eigenvectors (in 2 cases (Figure S4B), we chose eigenvector 4 instead of 3 when SMDD neurons had their maximal weight in eigenvector 4 instead of 3). These projections represent the time series of the latent variables and were termed principal components (PCs). Temporal PCs are the time integrals of PCs. The quiescent brain state in PCA space is not merely at zero but is offset by the activity of sleep-active neurons like the RMEs and RIS, which have a high weight on the first 3 eigenvectors. Phase plot trajectories are smoothed using a 3-sample sliding-average filter for visualization purposes.

Percentage of total variance explained

For comparing the percentage of total variance explained by each principal component (Figure 5C), we performed PCA as described above but restricted to the time periods that were determined active, thus sparing the quiescent time periods. We calculated the cumulative variance explained for the first 10 PCs from this analysis. Significance was determined using a resampling approach in MATLAB. We systemically resampled, without replacements, all possible combinations of pairs of datasets that can be drawn from a total of 12 recordings (n=6 for each WT fasted and WT starved), resulting in 461 possible combinations, excluding the actual dataset combination. We then calculated the mean cumulative frequency distributions for each group of resampled datasets and the L_1 distance (i.e. difference in the area under the curve (dAUC)) between them. The p-value indicates the fraction of combinations that resulted in a dAUC greater or equal to the difference between the experimental mean distributions.

Determining a neuron's principal active state

This was done as described previously (Nichols et al., 2017). Many neurons are known to be specifically active during either forward or reverse brain states. To determine each neuron's principal active state, we split the active brain state into reverse (when AVA was rising or high) and forward (when AVA was falling or low) brain states. The determination of the principal active state was done based on the distribution of $\Delta F/F_0$ during reverse and forward/turning states. Many neurons show high activity during one and low activity during the other state and were classified accordingly. Neurons with comparably high $\Delta F/F_0$ during both reverse and forward/turn states were classified as indiscriminative.

Mean activity distribution

For analysis of global neural activity (Figures 4A, 5D and 6D), all segmented neurons were included, except for neurons that responded to O_2 stimulation (BAG, URX, AQR, IL2). Dashed grey lines in Figures 4A and 6D indicate an inactivity cutoff: Manual inspection of all individual neural traces led to the conclusion that signals in neuronal time series with a mean $\Delta F/F_0$ value < 0.2 cannot clearly be distinguished from noise. To determine the cumulative frequency distributions of $\Delta F/F_0$ means for active and quiescent periods separately, composite traces were build that, for each neuron, consisted of all frames at either active or quiescent time points. The mean of each composite trace was calculated and these values were sorted and binned in increments of 0.06, resulting in 24 bins, and divided by the total number of data points to estimate the probability density function (PDF). We then calculated the cumulative sum of the PDF of each dataset separately; shown are the means (± SEM) across all datasets.

Calculation of mean $\Delta F/F_0$ for selected neurons (Figures 4C, 6F and S6A-S6C) was done by calculating the mean for composite traces of active and quiescent time periods for selected neurons. The respective active state for each neuron was defined by its principal state (see 'Determining a neuron's principal active state'). Data are presented as sorted from highest to lowest mean $\Delta F/F_0$ during the respective active state.

Calculation of mean $\Delta F/F_0$ of sensory neurons (Figures 4B and 6E) was performed as described for global $\Delta F/F_0$ calculations. Putative sensory neurons were assigned based on their position in the anterior region of the lateral ganglion, in which a majority of amphid sensory neurons are located (www.wormatlas.org). The most dorsal neuron included in the analysis was the unambiguously identified ASK neuron. The putative sensory neurons showed spontaneous activity that occurred largely uncorrelated with the global motor command state. The identification of most sensory neurons remained ambiguous.

Significance of active global mean distributions (Figure 5D) was determined as described above for 'Percentage of total variance explained'. We systemically resampled, without replacements, all possible combinations of pairs of

datasets that can be drawn from a total of 12 recordings (n=6 for each WT fasted and WT starved), resulting in 461 possible combinations, excluding the actual dataset combination. We then calculated the mean cumulative frequency distributions for each group of resampled datasets and the L_1 distance (i.e. difference in the area under the curve (dAUC)) between them. The p-value indicates the fraction of combinations that resulted in a dAUC greater or equal to the difference between the actual mean distributions. Significances of global mean distributions between active and quiescent periods (Figures 4A, 4B, 6D and 6E) were determined using a permutation test in MATLAB, by randomly placing quiescent blocks on each recording while maintaining the lengths of the original quiescent blocks to obtain two test cumulative distribution functions (CDFs), as for the original ones. This procedure was repeated 10^6 times for each dataset. For each iteration, we calculated the L_1 distance (i.e. absolute difference) between the two reshuffled CDFs. The p-value indicates the fraction of all iterations that resulted in a difference between 2 randomly reshuffled distributions at least as large as the original one.

RIS activity distribution

The graphs in Figure S6D display the distributions of all $\Delta F/F_0$ values for RIS during its principal active state (i.e. forward/turn) from all datasets in which RIS could be detected (WT fasted = 9, WT starved = 11, *daf-2* fasted = 10). For each genotype/condition, the histograms display the fraction of frames in which the logarithmically binned $\Delta F/F_0$ values were observed. Significance was determined by a custom resampling test in MATLAB. For each pairwise comparison, all forward/turn bout periods were pooled and the same number of bouts as originally observed for each genotype/condition were randomly re-assigned without replacements to calculate two test distributions. This procedure was repeated 10^6 times. For each iteration, we calculated the L_1-distance (i.e. the absolute difference) between the two resampled distributions. The p-value was calculated as the fraction of all iterations that resulted in a distance at least as large as the one measured between the original distributions. They were adjusted using the Bonferroni correction, i.e. by multiplying by the number of total pairwise comparisons performed.

Quantification of evoked responses in O_2-sensory neurons

Quantification of peak and sustained responses in BAG and URX sensory neurons was done by calculating, for each trace, the average $\Delta F/F_0$ over a 1-2 sec (peak) and 5 sec (sustainedness) interval of $\Delta F/F_0$ neural traces. As the time point of peak activity in URX neurons was variable the interval to quantify was individually determined for each trace (see also Figure S7).

ASK peak analysis

ASK peaks and corresponding amplitudes were detected as local maxima in $\Delta F/F_0$ ASK neural traces. Detected peaks were attributed to the quiescent or active brain state episodes according to their occurrence in time. Data are presented as mean amplitude per neuron.

Quantification and Statistical Analysis

For WT starved animals in the short-term experiments 28 experiments were performed in total. Figures S2C and S2D contain data from all these experiments while WT starved data used to generate Figures 1A-1D, S1A, S1D-S1E and S1F are subsets of these data, which are the WT control experiments performed in parallel to the other conditions. These overlapping data were usually not used in several panels. 3 data points occur in more than one of these figure panels because these experiments were performed as controls, and these exceptions are as follows: Figures S1D, S1E and S1F share three data point with Figures 1A-1D and one data point with Figure S1A. Note that Figures S1D, S1E, S1F show quantifications of different behaviors/time points from the same experiments. WT starved data used as controls for *daf-2* experiments (Figures 2A, 2B, S3A and S3C) represent an individual dataset for which animals were treated as their temperature-sensitive *daf-2* counterparts, as described in 'Worm population behavioral recordings'.
Most statistical tests were performed in GraphPad Prism 7, all resampling tests were performed using custom scripts in MATLAB. Details on the statistical test as well as exact details on sample size, displayed data and p-values can be found with each figure legend. In most cases, parametric statistical tests were used. If the n-number > 8, a D'Agostino-Pearson omnibus K2 test was performed in GraphPad Prism to test for normality. Subsequent test decisions were based on this. If more than 2 groups were compared, appropriate post-tests were performed. See also individual figure legends, which denote the respective post-test used. The individual method sections contain information on statistics when resampling tests were used. For tests performed in GraphPad Prism, a significance level of 0.05 was used. The experimenters were not blinded to the experimental conditions.

Raw data, worm strains, molecular biology constructs and MATLAB code are available upon request.

Supplemental References

Brockie, P.J., Madsen, D.M., Zheng, Y., Mellem, J., Maricq, A.V. (2001). Differential expression of glutamate receptor subunits in the nervous system of Caenorhabditis elegans and their regulation by the homeodomain protein UNC-42. J. Neurosci. *21*, 1510-1522.

Chartrand, R. (2011). Numerical differentiation of noisy, nonsmooth data. ISRN Applied Mathematics *2011*, 1-11.

Chelur, D.S., Chalfie, M. (2007). Targeted cell killing by reconstituted caspases. Proc. Natl. Acad. Sci. U.S.A. *104*, 2283-2288.

Hung, W.L., Wang, Y., Chitturi, J., Zhen, M. (2014). A Caenorhabditis elegans developmental decision requires insulin signaling-mediated neuron-intestine communication. Development *141*, 1767-1779.

Jansen, G., Thissjen, K.L., Werner, P., van der Horst, M., Hazendonk, E., Plasterk, R.H. (1999). The complete family of genes encoding G proteins of Caenorhabditis elegans. Nat. Genet. *21*, 414-419.

Kim, K., Sato, K., Shibuya, M., Zeiger, D.M., Butcher, R.A., Ragains, J.R., Clardy, J., Touhara, K., Sengupta, P. (2009). Two chemoreceptors mediate developmental effects of dauer pheromone in C. elegans. Science *326*, 994-998.

Mano, I., Straud, S., Driscoll, M. (2007). Caenorhabditis elegans glutamate transporters influence synaptic function and behavior at sites distant from the synapse. J. Biol. Chem. *282*, 34412–34419.

Nonet, M.L., Staunton, J.E., Kilgard, M.P., Fergestad, T., Hartwieg, E., Horvitz, H.R., Jorgensen, E.M., Meyer, B.J. (1997). Caenorhabditis elegans rab-3 mutant synapses exhibit impaired function and are partially depleted of vesicles. J. Neurosci. *17*, 8061–8073.

Ohno, H., Kato, S., Naito, Y., Kunitomo, H., Tomioka, M., Iino, Y. (2014). Role of synaptic phosphatidylinositol 3-kinase in a behavioral learning response in C. elegans. Science *345*, 313–317.